Topics in Current Chemistry (2022) 380:53
https://doi.org/10.1007/s41061-022-00406-5

REVIEW

Recent Advances in Semiconductor Heterojunctions and Z-Schemes for Photocatalytic Hydrogen Generation

Lion Schumacher[1] · **Roland Marschall**[1]

Received: 12 April 2022 / Accepted: 30 August 2022 / Published online: 21 October 2022

Abstract
The formation of semiconductor heterojunctions and Z-schemes is still a very prominent and efficient strategy of materials chemists to extend the absorption range of semiconductor combinations. Moreover, the spatial separation of photoexcited charge carriers and thereby the reduction of their recombination ultimately lead to increased photocatalytic activities. The present article reviews recent trends in semiconductor heterojunctions and Z-schemes with a focus on hydrogen generation and water splitting, exhibiting specific needs for charge carrier separation. We also included recent material trends, i.e. 2D/2D combinations, direct Z-schemes, MOFs and COFs, and combinations with upconversion materials.

Keywords Charge separation · Heterojunctions · Z-scheme · Photocatalysis · Hydrogen

1 Introduction

With an estimated market of 100 million metric tons, hydrogen (H_2) is an important basic chemical in industry and technology [1]. The worldwide most important process involving H_2 is the production of ammonia for the production of nitrogen-based fertilisers. Steam reforming of natural gas is by far the most dominant process employed to produce H_2 [2]. The literature describes and labels H_2 cleanness by different colours, the three main being grey, blue, and green. The "colour" of H_2 is determined by the source or additional technology utilised to produce the gas [3]. Since 96% of the overall H_2 is based on fossil fuels and mainly synthesised by steam reforming/water–gas shift reactions, a vast majority of H_2 is considered to be

This article is part of the Topical Collection "Solar-driven catalysis", edited by Nicolas Keller, Fernando Fresno, Agnieszka Ruppert and Patricia Garcia-Munoz.

✉ Roland Marschall
roland.marschall@uni-bayreuth.de

[1] Department of Chemistry, University of Bayreuth, 95447 Bayreuth, Germany

a polluting type of H_2, labelled grey H_2 [2–4]. Blue H_2 combines grey H_2 feedstocks with carbon capture and storage (CCS) technologies [4]. Whilst CCS technologies might defer climate change problems and buy time, H_2 production without the emission of greenhouse gases (green H_2) is considered to be the solution for decarbonising many large-scale chemical synthesis processes [4–6]. Promising technologies like fuel cells, the injection of H_2 in blast furnaces and several other technologies will need further research but rely first and foremost on the large-scale production of green H_2 [7–9]. An example of an environmentally friendly way to produce green H_2 is photocatalytic water splitting. Challenges like low solar-to-H_2 efficiencies as well as rare and expensive co-catalysts are yet to be solved [6]. Based on 50 years of materials research, this field has developed multiple strategies that will be essential to further improve photocatalysts in the future. Recent developments and improvements using two of these strategies—namely heterojunctions and Z-schemes—will be summarised in this review.

2 State of Research

2.1 H_2 Production and H_2 Economy

H_2 can be produced from a wide range of resources using different feedstocks, pathways and technologies, including renewable resources and fossil fuels [3]. Steam reforming is by far the most dominant process employed to produce H_2 for industrial purposes. This method uses a mix of light hydrocarbons with methane being the dominant one. In the case of natural gas, a desulphurisation step is necessary to convert sulphur into H_2S, which is then adsorbed and removed. For the actual steam reforming, the gas mix of high-temperature steam and desulphurised feed is exposed to a nickel-based catalyst at high pressure. Depending on the process design, temperature ranges of 750–900 °C and pressure ranges of 3–25 bar are used to convert hydrocarbon and steam into synthesis gas consisting of a mix of CO and H_2 [2]:

$$C_xH_y + xH_2O \rightleftharpoons xCO + \left(x + \frac{y}{2}\right)H_2 \tag{1}$$

The steam-reforming reaction (reaction (1)) for the formation of CO and H_2 is endothermic and therefore requires heat. External heating can be avoided or reduced by using a compact design and the exothermic partial oxidation of the feedstock (reaction (2) and (3)) [2]:

$$C_xH_y + \left(\frac{x}{2} + \frac{y}{4}\right)O_2 \rightleftharpoons xCO + \frac{y}{2}H_2O \text{ (thermal reaction)} \tag{2}$$

$$C_xH_y + \frac{x}{2}O_2 \rightleftharpoons xCO + \frac{y}{2}H_2 \quad \text{(catalytic reaction)} \tag{3}$$

However, efficient heat recovery is essential to enable an economic operation of the process. The H_2:CO ratio in the resulting synthesis gas can be adjusted via the

water–gas shift reaction (reaction (4)), which is exothermic for the formation of CO_2 and H_2 and allows lower temperatures than the steam reforming reaction [2].

$$CO + H_2O \rightleftharpoons CO_2 + H_2 \quad (4)$$

Depending on the subsequent use, the gas mix is subjected to separation processes like pressure swing adsorption (PSA), membrane processes, or methanation of left-over CO.

According to reactions (1) and (4), steam reforming can produce up to four units of H_2 gas for each unit of methane. While natural gas is the most common feedstock for steam reforming, other fossil fuels can usually be converted to lighter hydrocarbons. Gasification can be applied to all solid and liquid carbon-containing feedstocks, including biomass. As a result, the gasification of coal has a significant contribution to global greenhouse gas emissions considering the coal-based production of ammonia and methanol [2, 10].

Only a small amount of the overall produced H_2 stems from electrochemical processes. Nonetheless, electrolysis might be a key technology since it allows the production of pure H_2 from water while using electrical energy from renewable energy sources like wind power or photovoltaic. One distinguishes between alkaline, PEM (proton-exchange membrane), and high-temperature electrolysis. Alkaline electrolysis is a well-established production method reaching high overall efficiencies in the order of 70–80%. At temperatures between 60 and 90 °C, H_2 is co-generated with oxygen (O_2) [2]. Water splitting electrolytic processes are closely related to the respective fuel cell technology. High-temperature electrolysis, for example, uses the principles of inverted solid oxide fuel cells (SOFC). The energy required for the process is partially supplied as heat, leading to a lower electricity consumption compared to the other mentioned processes [2, 11].

In comparison, the price of electricity and natural gas largely defines the competitiveness between steam reforming and electrolysis. The production of H_2 via alkaline electrolysis is often considerably more expensive than the production by steam reforming [2, 11].

While electrolysis is a well-known method to purposely produce H_2, other chemical or electrolytic processes produce H_2 as a side product. One example is the electrolytic production of chlorine. Common processes use membrane or diaphragm cells and produce H_2 at the cathode. In this context, the co-production of H_2 is often seen as a waste of energy and a safety hazard. Therefore, present developments aim at process modifications that reduce or eliminate H_2 co-production. O_2 depolarised cathodes are, for example, used since the beginning of this millennium. Here, O_2 is reduced together with water to hydroxide ions, which enables a reduction in cell voltages of up to 30% [2, 12, 13].

H_2 is used for fertiliser production, petrochemical refining, metal work, food processing, power generator cooling in power plants, and semiconductor manufacturing [3]. Hence, H_2 is a basic substance for many industrial processes in the twenty-first century. Additionally, the term "H_2 economy" is often used to describe ideas and challenges about a future economy heavily relying on H_2 [4, 14–17]. The concept of H_2 economy was originally created by John Bockris in the 1970s. It described a

vision in which H_2 is produced via water electrolysis, transported via pipelines and eventually converted back to electricity in fuel cells [18]. The idea of using H_2 as a fuel dates back to the beginnings of fuel cell developments by W.R. Grove in 1839. Even science fiction writings from the nineteenth century discussed H_2/water as an energy source (Jules Verne, "The Mysterious Island") [14]. Nowadays, there are still different opinions on whether H_2-based technologies will play a major role in a certain sector or will be outperformed by other technologies. Nevertheless, recurring statements about the future role of H_2 and its production are found in literature. While publications from the early 2000s still partially discuss a H_2 economy based on fossil fuels, nuclear reactors and renewable energy sources, publications from the last decade focus mainly on green H_2 [4, 14]. Green H_2 is seen as a solution to decarbonise many large-scale chemical synthesis processes [4]. It is also seen as an energy carrier and a storage medium for the intermittency of many renewable resources [15]. In this context, decentralisation and microgrids are discussed [4]. At the same time, H_2 is often no longer evaluated in isolation but in conjunction with various alternatives. The term "H_2 economy" may therefore be misleading but illustrates that (green) H_2 will play an important role to enable a society supported entirely by renewable energy [4, 14–17].

2.2 Photocatalytic Water Splitting

With growing attention being paid to reducing greenhouse gas emissions, renewable resources rapidly gain potential as a clean source to produce renewable H_2 as a carbon-emissions-free energy carrier [3]. Solar energy can be seen as the most abundant renewable energy source. Therefore, H_2 production from solar energy is considered to be a promising solution for sustainable energy [19].

Semiconductor materials can convert sunlight energy into chemical energy by catalysing the formation of chemical bonds. Thus, generating H_2 and O_2 by performing photocatalytic water splitting is intensely investigated [20–23]. A semiconductor absorbs sunlight when the energy of the incident photon is equal to or larger than the band gap (E_g). An electron is thereby excited from the valence band (VB) into the conduction band (CB) of the semiconductor (Fig. 1). Together with the remaining hole in the VB, an exciton is formed [20].

The photoexcited electron can be used to reduce protons to H_2 if the CB minimum has a more negative potential than the electrochemical potential of reaction (5). Similarly, the photogenerated hole in the VB can perform the electrochemical oxidation of water to O_2 if the maximum of the VB is more positive than the electrochemical potential of reaction (6) [20, 23]:

$$2H^+ + 2e^- \rightarrow H_{2(g)} \quad \Delta E^0 = +0.41\ \text{V at pH 7} \tag{5}$$

$$H_2O + 2h^+ \rightarrow 0.5O_{2(g)} + 2H^+ \quad \Delta E^0 = +0.82\ \text{V at pH 7} \tag{6}$$

Compared to the H_2 evolution reaction (HER), the O_2 evolution reaction (OER) is comparatively more complex because this reaction requires a four-electron oxidation

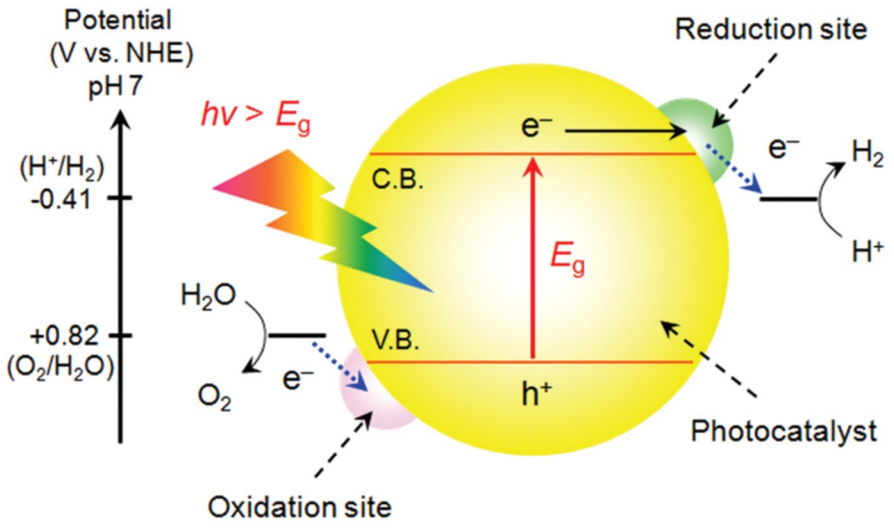

Fig. 1 Schematic energy diagram of photocatalytic water splitting; oxidation site and reduction site might refer to co-catalysts discussed in the next section. Reprinted with permission from [24] © 2010 American Chemical Society

step combined with the removal of four protons to form a relatively weak oxygen–oxygen bond [25]. The overall water splitting reaction is an uphill reaction with a positive shift in Gibbs free energy (+237 kJ/mol). Therefore, water splitting is thermodynamically a photosynthetic reaction [26]. In theory, the minimum band gap energy (E_g) of the semiconductor should be 1.23 eV (approximately equivalent to a wavelength of 1000 nm). Due to energy losses, kinetic overpotentials are needed; thus, the E_g of a single semiconductor should lie in the range of 1.5–2.5 eV [23].

It is known that the CB potential of a semiconductor material in aqueous solutions usually exhibits a pH dependence according to the following equation [23]:

$$E_{CB} = E^0_{CB}(\text{pH } 0) - 0.059 \text{ pH}$$

Since the redox potentials of water show the same linear dependence with a slope of 0.059 V per pH, band edge positions of the semiconductor usually cannot be shifted relative to the redox potentials of water by changing the pH value [23].

2.3 Strategies for the Improvement of Photocatalysts

2.3.1 Single Absorber, Co-catalysts and Sacrificial Agents

So far, many semiconductors have been found to be capable of producing H_2 or O_2 under light irradiation [23, 27, 28]. Thereby, metal oxide semiconductors can usually be divided into two classes: materials containing metal cations with d^0 configuration and those with d^{10} configuration [6, 23]. Many recent research activities are focused on composite materials, but single absorbers are still investigated. This

is due to newly discovered materials or known materials that are back in the focus of research. One example is $SrTiO_3$ which experienced a renaissance due to new insights into defect engineering and the electronic structure of doped $SrTiO_3$ [6, 29–31].

Charge carrier recombination limits photocatalytic efficiencies in many photocatalytic systems but especially for undecorated semiconductors used as photocatalysts. Increasing the crystallinity of a photocatalyst can reduce recombination. Defects and grain boundaries are related to interband and surface states, which act as traps for holes. Therefore, increasing the crystallinity can result in higher photocatalytic efficiencies [20]. Another possibility to prevent charge carrier recombination is charge separation. One popular strategy is the use of co-catalysts often applied as nanoparticles on the surface of a semiconductor photocatalyst. The Fermi energy of the metal nanoparticle is usually lower than that of the semiconductor, facilitating electron transfer from the semiconductor to the metal via a Schottky contact [20]. Usually noble metal nanoparticles such as rhodium, palladium, platinum or gold are used. Noble metals serve as electron sinks, thus spatially separating the electron from the photoexcited hole in VB of the semiconductor [20, 32]. Besides noble metals as co-catalysts for the reduction reaction, other materials like metal oxides (RuO_2, NiO, CuO/Cr_2O_3, $Rh_{2-y}Cr_yO_3$), metal sulphides (MoS_2) and molecular co-catalysts have been investigated [20, 32–35]. For the oxidation reaction, metal oxides such as RuO_2 and IrO_2 are used. Efforts are being made to use more earth-abundant alternatives for both the reduction and the oxidation reaction [20, 32]. Charge carrier separation due to co-catalysts can also stabilise certain photocatalysts since some sulphides, oxysulphides, oxynitrides and nitride semiconductors are known for their photoinstability, which is usually due to photocorrosion. Therefore, loading of oxidation cocatalysts like PdS can protect semiconductors that tend to be oxidised by photogenerated holes [32, 36].

As already mentioned, the reduction and oxidation of water is a complex multistep reaction involving four electrons. Thus, photocatalytic water splitting is a rather inefficient process and far away from large-scale industrial applications. Using electron donors can improve the H_2 production as holes are scavenged by these molecules. Additionally, charge carrier recombination can be reduced and the back reaction to water is supressed because O_2 is not produced [37]. Various organic and inorganic compounds (alcohols, organic acids, hydrocarbons, sulphides and sulphites) are being employed as hole scavengers/electron donors [28, 37]. Methanol is one of the most frequently used sacrificial agents. Nonetheless, the application of methanol is highly debatable for environmental reasons even if the substance is derived from biomass. Furthermore, molecular H_2 formation in systems using sacrificial agents should not be called water splitting. The term water splitting should only be used when pure water is used as solvent and reactant, without any additional reagents [6]. Acting as an electron donor, methanol reacts irreversibly with the photogenerated VB holes (Fig. 2) [37]. In the overall methanol decomposition reaction (not shown in Fig. 2), methanol can be stepwise oxidised to carbon dioxide [38].

Similarly, sacrificial electron acceptors can be used to support the oxidation of water. Silver cations, Ag^+, are employed by a vast majority of research groups. The photocatalytic formation of molecular O_2 is accompanied by the reduction of Ag^+

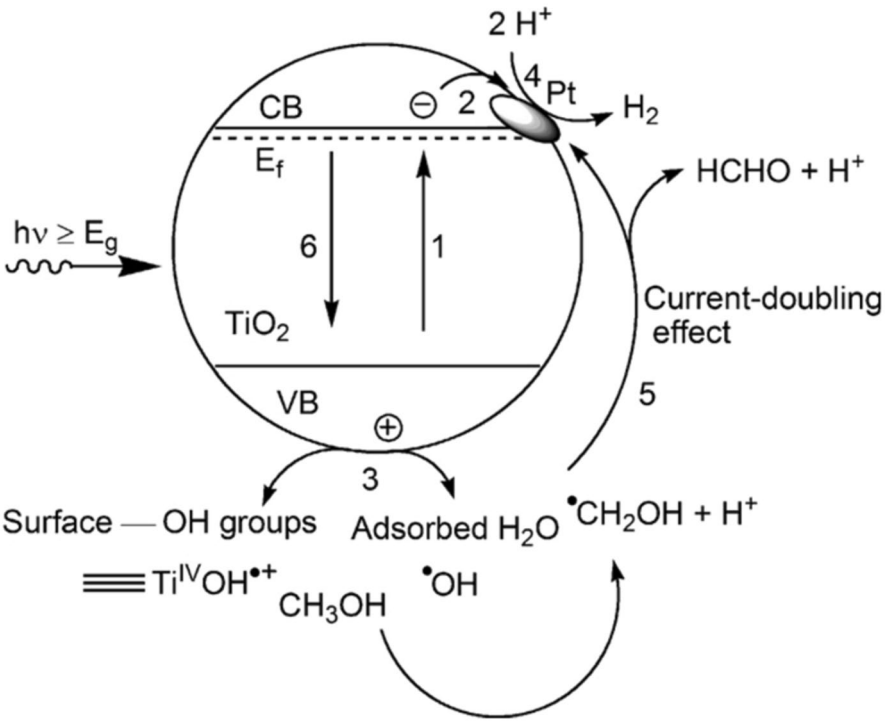

Fig. 2 Schematic representing the proposed steps for the photocatalytic molecular H_2 production from aqueous methanol solution, (1) photogeneration of charge carriers, e^- and h^+; (2) trapping of e^- by Pt islands; (3) first oxidation step of CH_3OH by either trapped hole or hydroxyl radical, $^{\bullet}OH$; (4) reduction of H^+; (5) formation of HCHO through e^- injection into the conduction band of TiO_2 or to the Pt islands (current-doubling); (6) recombination channel. Reprinted with permission from [39] © 2011 Elsevier

and thereby accompanied by the deposition of metallic silver nanocontacts. The optical changes and changes in catalytic activity arising from this deposition should always be discussed [37].

2.3.2 Heterojunctions

Key issues for improving photocatalytic activity are improved light absorption, high crystallinity, large surface areas, and effective charge separation. Furthermore, suitable band positions are needed, as well as earth-abundant elements and high chemical stability of the photocatalyst [20]. A composite photocatalyst system consisting of two or more semiconductors allows different favourable properties from each participating compound to be combined, extending the absorption range of the visible spectrum, reducing photoexcited electron hole recombination and increasing the photo-corrosion stability, thus improving water splitting efficiency [40–43].

Heterojunctions formed by two semiconductors can be classified into three different types depending on the band position (Fig. 3).

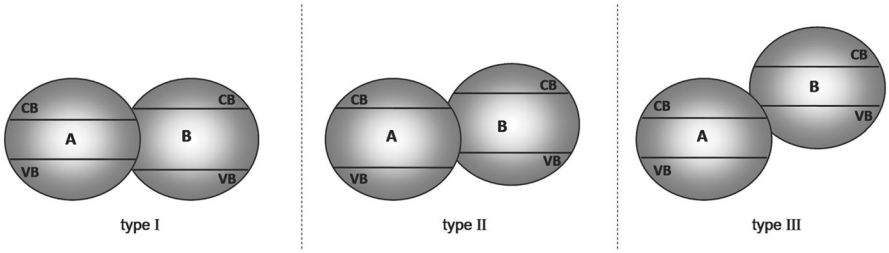

Fig. 3 Different types of semiconductor heterojunctions. Reprinted with permission from [20] © 2013 Wiley-VCH

In type I heterojunctions, material A has a smaller band gap than material B. Due to a more negative CB and a more positive VB of material B, holes and electrons transfer from material B to material A. An example of a type I heterojunction is TiO_2/Fe_2O_3 where photogenerated electron and hole flow occurs from TiO_2 to Fe_2O_3 [40, 44, 45]. A type I heterojunction yields therefore no improvement to charge carrier separatio and thus, in theory, no improvement in photocatalytic activity. Due to many wide band gap semiconductors known and limitations in valence band and conduction band positions, type I heterojunctions are common when composite materials consist of a small band gap and a wide band gap semiconductor [20, 40, 46].

In type II heterojunctions, the CB position of material B is more negative than that of material A, while material A has a more positive VB position. As a result, electrons and holes transfer in opposite directions, which leads to improved charge carrier separation, reduced recombination probability, increased charge carrier lifetimes, and, in the end, to improved photocatalytic activity. Most of the examples of composite photocatalysts described in the literature are type II heterojunctions. A $WO_3/BiVO_4$ heterojunction is one example of this type of system [20, 40, 47].

In type III heterojunctions the charge carrier transfer is the same as in type II semiconductors, but the band positions are further set off. Due to the band position, these systems are also called broken-gap situations [20]. A BP/ReS_2 system (BP = black phosphorus) is one example of this type. In general, type III heterojunctions are rather rarely reported but for example discussed for electronic applications [48].

2.3.2.1 Recent Trends in Heterojunction Photocatalysts Tremendous efforts have been dedicated to the development of type II heterojunction photocatalysts due to their ability to separate photogenerated electrons and holes. However, in the past few years, a trend towards Z-schemes (next section) can be observed. Broad review articles discussing improvements in heterojunction photocatalysts have usually been written in 2017 or earlier [20, 47, 49, 50]. Recent review articles are rare and heterojunctions are rather discussed in articles that only cover one specific material. However, there are recent trends that are worth mentioning.

Photocatalysts made of 2D materials are of particular interest due to their electrical and optical properties. Type II heterojunctions based on 2D materials have been

designed and studied as efficient photocatalysts theoretically and experimentally [51–55]. Hua et al., for example, reported a 2D $La_2Ti_2O_7/In_2S_3$ type II heterojunction [52]. The intimate contact of the two layers was realised by strong Coulomb static forces due to inverse zeta potentials of both components. The strong interaction between the two layers and the type II heterojunction co-promoted the charge separation, resulting in H_2 production rates 3.5 times higher than pristine In_2S_3 and 18 times higher than the physical mixture of both components [51, 52]. Although type II heterojunctions can separate photoinduced charges efficiently, *p-n* heterojunctions can separate the charges even faster with the aid of internal electric fields [51].

In 2018, Qin et al. constructed a *p-n* heterojunction by attaching *p*-type Cu_3P nanoparticles to the surface of *n*-type g-C_3N_4. The photocatalyst exhibited 95 times higher hydrogen evolution activity from 10 vol% triethanolamine (TEOA) solution than bare g-C_3N_4 with an apparent quantum efficiency of 2.6% at 420 nm [56]. Two years later, a MoS_2/Bi_2O_3 *p-n* heterojunction for overall water splitting was described. Bi_2O_3 nanorods were anchored on MoS_2 microflowers. As a result, H_2 evolution rates increased by a factor of ten [57].

Qin et al. prepared a 2D/2D g-$C_3N_4/ZnIn_2S_4$ heterojunction photocatalyst [58]. The improved photocatalytic performance (6.095 mmol g^{-1} h^{-1} using triethanolamine as sacrificial agent) was attributed to the larger contact area and sulphur vacancies that acted as active sites for trapping electrons, which led to elongated charge lifetimes. Furthermore, the vacancies shortened the band gap, enhancing the absorption of visible light. Van der Waals (vdW) forces acted as an intermolecular driving force for charge carrier transport. This was considered to be an alternative route for enhancing H_2 evolution efficiency since heterojunctions are therefore not restricted by the lattice matching of the component materials [58].

A similar approach was used by Zeng et al. for theoretical description of a SiH/CeO_2(111) type II heterojunction [59]. Both components were chosen because of a $< 1\%$ lattice mismatch. The staggered band structure (Fig. 4) demonstrates that SiH/CeO_2(111) is a type II vdW heterojunction, which effectively promotes the separation of photogenerated hole-electron pairs and should improve its photocatalytic activity.

The band gap of the SiH/CeO_2(111) heterojunction is 2.64 eV and thus smaller than the band gap of the SiH monolayer and CeO_2(111). Light absorption of the composite material should be significantly extended into the visible light wavelength range compared to that of pure CeO_2(111), and oxygen vacancies on the surface of CeO_2(111) can also enhance its visible light absorption performance. Moreover, valence band maximum (VBM) and conduction band minimum (CBM) potentials meet the requirements of water splitting (Fig. 4) [59]. Simulations like these might help to synthesise deliberately chosen composite materials in the future.

Deep investigations might explain and solve problems that have limited the performance of (heterojunction) photocatalysts in the past. For example, it is known that certain *p*-type materials can be used as photocathode materials for H_2 evolution, but only show low activity as photocatalysts. Zhao et al. investigated *p*-type gallium phosphide to better understand this limitation [60]. H_2 evolution rates could be inversely correlated with the standard reduction potential of the used donors (KI,

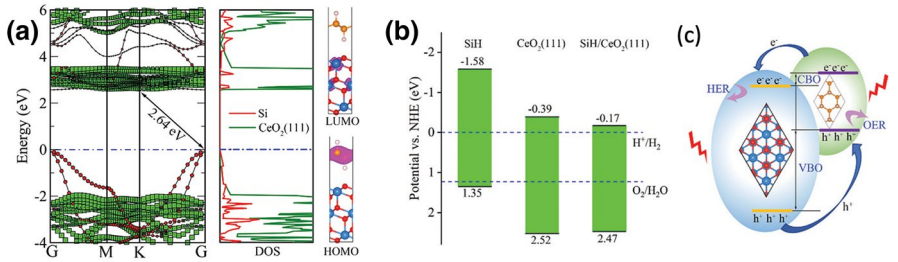

Fig. 4 **a** Electronic structure of the SiH/CeO_2(111) heterojunction. The projected band structure (left panel), partial density of states (PDOS, middle panel), as well as the highest occupied molecular orbital (HOMO) and lowest unoccupied molecular orbital (LUMO) (right panel). The green squares and red circles in the left panel represent the CeO_2(111) and SiH constituents, respectively. The Fermi level is set to zero. **b** Calculated VBM and CBM potentials versus normal hydrogen electrode (NHE) of SiH, CeO_2(111), and SiH/CeO_2(111) heterojunction. The upper and lower blue dashed lines stand for the proton reduction potential (H^+/H_2) and O_2 reduction potential (O_2/H_2O) for water splitting with values of 0 and 1.23 eV (pH 0), respectively. **c** Schematic diagram of charge transfer between SiH/CeO_2(111) heterojunction layers. Reprinted with permission from [59] © 2021 Royal Society of Chemistry

$K_4[Fe(CN)_6]$, Na_2SO_3; more reducing donors give lower rates). Due to a depletion layer at the *p*-type gallium phosphide/electrolyte interface, photogenerated electrons are directed away from the cocatalyst (here Ni_2P) toward the sacrificial donors and surface states (Fig. 5).

The electrons react with the surface states or with the oxidised form of the sacrificial electron donor (e.g. triiodide is reduced to iodide). As a result, electrons deep inside the *p*-type semiconductor must reach the cocatalyst by diffusion. This is a slow process because electrons are the minority carriers with a short lifetime. According to surface photovoltage measurements, the depletion layer had a barrier

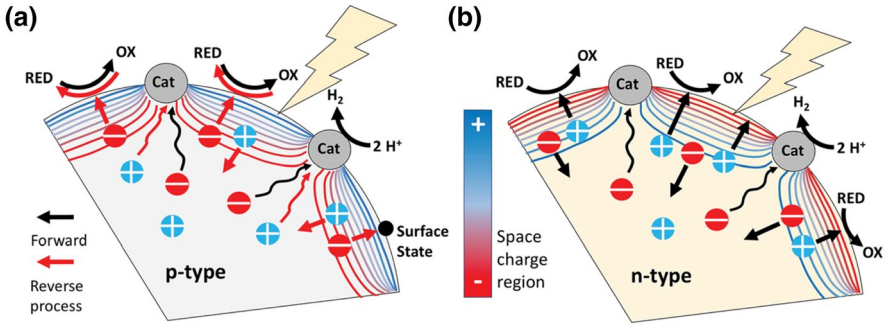

Fig. 5 Depletion layer and charge carrier movement in illuminated **a** *p*-type and **b** *n*-type semiconductor/co-catalyst configurations in aqueous solutions of a reducing sacrificial agent. Straight arrows indicate drift and wavy arrows indicate diffusion. Minority carriers (holes for *n*-type SC and electrons for *p*-type SC) generated inside the depletion layer are attracted to the surface and away from the proton reduction co-catalyst (Cat). For *p*-type semiconductors this promotes the back reaction (red arrows) and for *n*-type semiconductors the forward reaction (black arrows). Reprinted with permission from [60] © 2021 Royal Society of Chemistry

height of up to 0.45 eV for Na_2SO_3. Findings like these explain basic observations in semiconductor photocatalysis and might play a key role in the development of *p*-type and composite photocatalysts [60].

In recent years, the number of examples for heterojunctions with three type of absorber materials has significantly increased. One of the earliest examples for such a triple heterojunction was the combination of anatase-TiO_2/rutile-TiO_2/WO_3 [61]. Instead of WO_3, Huang et al. used carbon nitride in combination with anatase-TiO_2 and rutile-TiO_2, increasing the visible light absorption further for H_2 and O_2 evolution [62]. Other triple absorber heterojunctions reported including TiO_2 are for example Fe_2TiO_5/Fe_2O_3/TiO_2 [63], Ag_2O/Fe_2O_3/TiO_2 [64], and Bi_2O_3/C_3N_4/TiO_2 [65].

An interesting example is the combination of CoP/CdS/WS_2, containing no oxide at all forming a *p-n-n* heterojunction for H_2 generation [66]. The apparent quantum efficiency at $\lambda = 420$ nm was reported to be 1.34%; unfortunately, no oxidation product was confirmed in pure water. Containing two other sulphide materials, ZnS/CdS/TaON heterojunctions were reported to show 14 times higher H_2 evolution activity (from sulphide/sulphite solutions) compared to CdS/TaON, in the absence of noble-metal co-catalysts and an optimum amount of ZnS of 6 wt% [67]. Overall, 839.6 μmol h^{-1} g^{-1} could be reached under AM 1.5G illumination; no quantum efficiencies were reported. Since ZnS has quite a large band gap compared to CdS and TaON, ZnS might act as a hole sink/co-catalyst rather than an absorber in such a system. CdS on the other hand is very prominent for its ideal band gap for water splitting but well-known photocorrosion issues. In combination with $Bi_{20}TiO_{32}$ and $Bi_4Ti_3O_{12,}$ it was reported as ternary heterojunction for H_2 evolution recently [68]. Photocatalytic H_2 production (from aqueous methanol solution) of up to H_2 production 1890 μmol g^{-1} h^{-1} under 250-W xenon lamp ($\lambda > 400$ nm) illumination was reported, with strongly increased activities compared to $Bi_4Ti_3O_{12}$, CdS, or $Bi_{20}TiO_{32}$/$Bi_4Ti_3O_{12}$. However, not a heterojunction behaviour but a scheme involving a type I bridged coupled Z-scheme system was proposed to explain the observed activities. Z-schemes will be covered in the following section.

2.3.3 Z-Schemes

Z-schemes use two different semiconductors and typically a reversible donor/acceptor pair, a so-called shuttle redox mediator (Fig. 6). This system is inspired by natural photosynthesis in green plants, where photosystems I and II harvest 700 and 680-nm photons, respectively [69].

A traditional Z-scheme photocatalyst was first proposed by Bard in 1979 [70]. Since then, redox couple mediated Z-schemes have attracted considerable attention. In contrast to heterojunctions, the semiconductors are usually not in direct contact to each other but electronically coupled via the redox mediator (the next section will concentrate on solid Z-schemes). Thus, semiconductors can be combined that can only perform either water reduction or oxidation due to their band potential [69]. For example, WO_3, which does not have the ability to reduce H^+, is capable of producing O_2 from an aqueous solution containing appropriate electron acceptors under

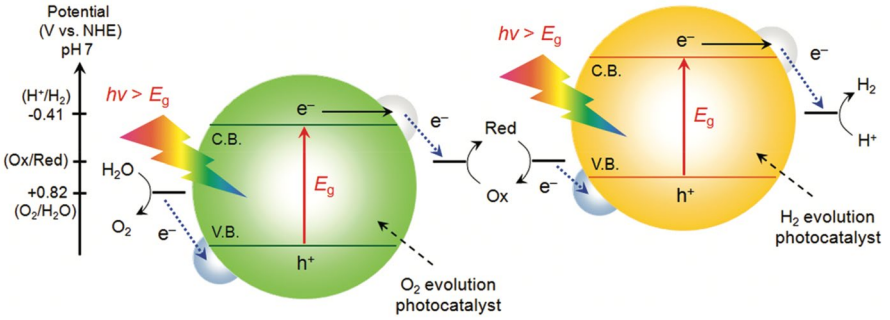

Fig. 6 Schematic energy diagram of photocatalytic water splitting for a two-step photoexcitation system. Reprinted with permission from [24] © 2010 American Chemical Society

visible light and acts as an effective building block for O_2 evolution in Z-scheme water splitting [69].

The redox mediator is an essential component in the Z-scheme water splitting system because it transfers electrons from an O_2 evolution photocatalyst to a H_2 evolution catalyst. Therefore, the flow of charge carriers is reversed in Z-schemes compared to the above mentioned heterojunctions of two semiconductors [6]. The process leads to spatially separated, high-redox-capacity electrons and holes in the H_2 evolving photocatalyst and the O_2 evolving photocatalyst, respectively.

The most employed redox couples are Fe^{3+}/Fe^{2+} and IO_3^-/I^-, which both have unique characters affecting the efficiency of Z-scheme water splitting. The following reactions describe a water splitting system using the IO_3^-/I^- couple as a mediator [69]:

$$I^- + 3H_2O + 6h^+ \rightarrow IO_3^- + 6H^+ \tag{7}$$

$$2H^+ + 2e^- \rightarrow H_{2(g)} \tag{8}$$

$$IO_3^- + 6e^- + 3H_2O \rightarrow I^- + 6OH^- \tag{9}$$

$$2H_2O + 4h^+ \rightarrow O_{2(g)} + 4H^+ \tag{10}$$

Taking the IO_3^-/I^- couple, there is a dependence of activity on the concentration of the redox mediator. With increasing the concentration of I^-, the efficiency of the I^- oxidation by VB holes in a H_2 evolution photocatalyst is enhanced, while the oxidation reaction in the O_2 evolution site is suppressed because of competitive oxidation of I^- by photogenerated holes in the VB of the O_2 evolution photocatalyst. Hence, using NaI as an initiator, there is a volcano-type trend between the concentration of NaI and Z-scheme activity in most cases [69, 71–73].

An Fe^{2+}/Fe^{3+} redox system is limited to acidic conditions because iron ions undergo precipitation (iron hydroxide) in neutral and basic conditions. The

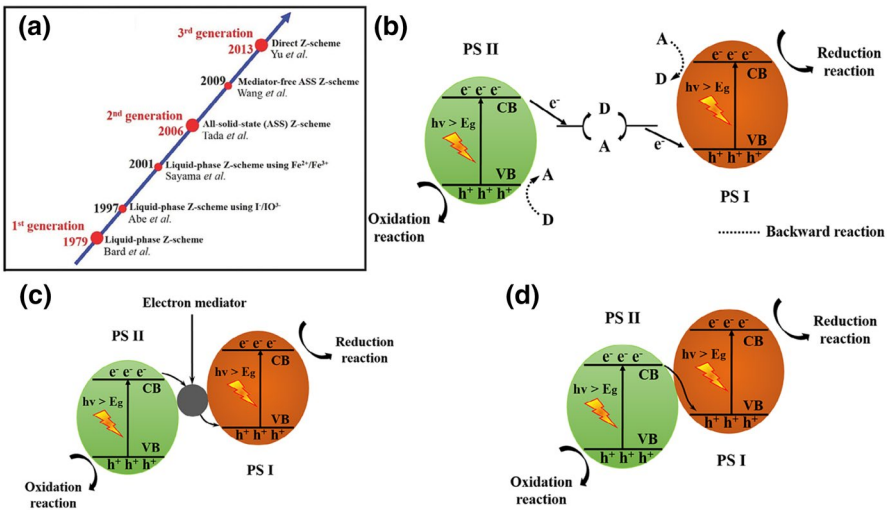

Fig. 7 **a** The roadmap of the evolution of the Z-scheme photocatalytic system from the first generation to the third generation. **b** Schematic illustration of electron transfer in a traditional Z-scheme photocatalytic system (PS I-A/D-PS II), where A and D represent the electron acceptor and donor, respectively. **c** Schematic illustration of electron transfer in an all-solid-state Z-scheme photocatalytic system with an electron mediator (PS I–EM–PS II), where EM represents the electron mediator that provides an electron transport channel. **d** Schematic illustration of electron transfer in a direct Z-scheme photocatalytic system without any electron mediator (PS I–PS II). Reprinted with permission from [78] © 2020 Wiley-VCH

IO_3^-/I^- couple can be employed in a wider range of pH values but also shows a pH dependence [69].

Apart from their role of shuttling electrons, redox mediators show multiple side effects in Z-scheme water splitting. One example is that I^- ions apparently undergo adsorption onto the surface of Pt, used as a co-catalyst, forming an iodine layer which suppresses the backward reaction of water formation [69, 74]. A similar behaviour was reported for the Fe^{2+}/Fe^{3+} redox mediator. Water formation and the reduction of Fe^{3+} are efficiently suppressed by adsorption of $[Fe(SO_4)(H_2O)_5]^+$ and/or $[Fe(OH)(H_2O)_5]^{2+}$ on Pt surfaces [69, 75]. Although the backward reaction of water formation on Pt is not completely suppressed by adsorbed iron species, further studies revealed that Ru does not suffer from water formation. Using Ru as a co-catalyst, the reduction of Fe^{3+} by H_2 and the oxidation of Fe^{2+} by O_2 are also suppressed [69, 76].

However, traditional Z-scheme photocatalysts have further drawbacks. Noteworthy are light-shielding effects by the redox mediator, slow charge carrier transfer rates limited by diffusion of ion pairs, and, as already mentioned, limitations because of pH sensitivity. Moreover, redox mediators are often unstable and tend to deactivate, which results in decreased reaction rates [77]. In addition, the photogenerated electrons in the CB of the photocatalysts I (PS I) and holes in the VB of photocatalysts II (PS II) with strong redox ability can also be consumed by the redox mediator (Fig. 7). This is called backward reaction and again has a negative impact on the photocatalysis [78, 79]. Several attempts have been made

to overcome these drawbacks. The historical evolution of Z-scheme photocatalysts is shown in Fig. 7.

2.3.3.1 All-Solid-State Z-Schemes, Direct Z-Schemes In 2006, Tada et al. proposed the concept of an all-solid-state Z-scheme heterojunction. The CdS-Au-TiO_2 system used gold as a solid-state electron mediator [80]. As shown in Fig. 7c, the photocatalytic system consists of two semiconductors and a solid-state electron mediator between two semiconductors with an intimate contact. The intimate contact between the mediator and both semiconductors favours the interfacial charge carrier transfer [77, 78]. Commonly used solid-state electron mediators are noble metal (such as Au, Ag, Cu, Pt) shells/nanoparticles and graphene and carbon nanotubes. When the two semiconductors are excited by light irradiation, the photogenerated electrons in the CB of PS II can recombine with the photogenerated holes in the VB of PS I with the help of the electron mediator because of low contact resistances with both semiconductors [78, 81].

All-solid-state Z-schemes eliminate the aforementioned backward reactions and the long-term stability issues of redox mediators in traditional Z-schemes. Furthermore, it can be applied in liquid and gas phases because of the solid conductor [77, 78]. Light-shielding effects can be reduced compared to traditional Z-scheme photocatalytic systems, but effective light utilisation might be hindered by light absorption from the electron mediator. These conductors might also act as co-catalysts instead of charge-transfer shuttles. Therefore, intimate contact and carefully designed sandwiched structures are necessary, which is synthetically challenging. Additionally, the use of rare and noble metals limits practical applications of all-solid-state Z-schemes [77, 78, 82].

In 2013, a direct Z-scheme heterojunction (g-C_3N_4/TiO_2) without using any electron mediator was reported by Yu et al. [83]. In contrast to the traditional Z-scheme system, the backward reactions were significantly suppressed because of the absence of redox mediators. The shielding effect caused by redox mediators/charge carrier mediators can also be reduced [77].

Analogous to the all-solid-state Z-scheme, the directly contacted semiconductors are both exited by light irradiation, and the photogenerated electrons in the CB of PS II can recombine with the holes in the VB of PS I. As a result, the photogenerated electrons in CB of PS I and photogenerated holes in the VB of PS II are spatially separated and maintain their strong redox capability [78]. A work function difference between the two semiconductors is a pre-requisite for the Z-scheme charge transfer mode. PS I must have higher CB and VB positions and a smaller work function (higher Fermi level) than PS II. When both semiconductors are in contact, an electron transfer from PS I to PS II takes place due to Fermi level equilibration (c.f. the *n-n* type direct Z-scheme in Fig. 8). Thus, the PS I side is positively charged, whereas the PS II side is negatively charged. Hence, an internal electric field (IEF) as well as band bending occurs. PS II energy band edges bend downwards because the accumulation of electrons and PS I energy band edges bends upwards because of decreased electron density [77, 82]. The IEF, the extra potential barrier induced by band bending, and Coulomb repulsion

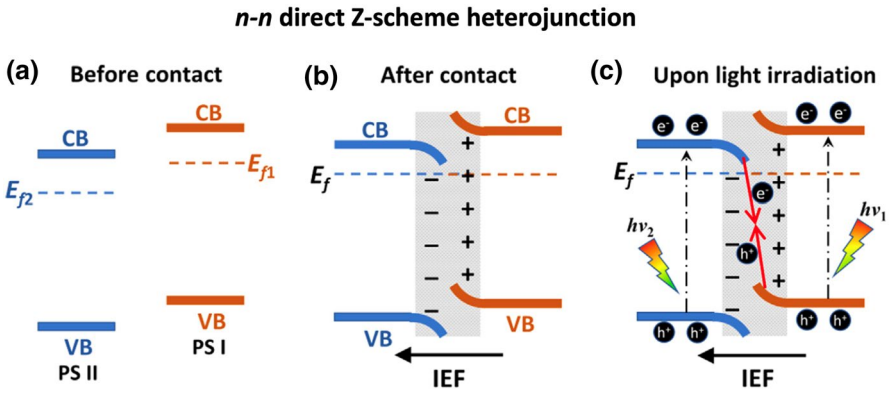

Fig. 8 Schematic of *n–n* type heterojunction: **a** before contact, **b** after contact, and **c** formation of direct Z-scheme charge transfer upon light irradiation. E_f and IEF stand for Fermi level and internal electric field, respectively. Reprinted with permission from [82] © 2021 Elsevier

hinder photogenerated electrons from transferring from PS I CB to PS II CB. This also applies to the photogenerated holes in PS II VB [77].

A similar process occurs in the construction of a *p-n* type direct Z-scheme. However, when the Fermi level of a *p*-type semiconductor (*p*-PS) is lower than that of an *n*-type semiconductor (*n*-PS), a type II heterojunction is formed. The energy band edges are bent in an inverted fashion at their interface (Fig. 9). Therefore, under light irradiation, photogenerated electrons move from *p*-PS to *n*-PS and holes in the opposite way driven by the IEF. The requirement for Fermi levels is easily met in *n-n* type heterojunctions but very hard to fulfil in *p-n* heterojunctions because of the huge band offset (Fig. 9). Hence, most direct Z-schemes are made of *n-n* heterojunctions [82].

Known *p-n* type direct Z-schemes are for example $CuInS_2$–WO_3, $CuAl_2O_4$–Bi_2WO_6, and Cu_2O–TiO_2 [82, 84–86].

The band alignment configuration in Z-scheme heterojunctions is similar to that of type II heterojunctions, but their charge transfer mechanisms are different. To investigate the exact charge transfer process, various methods can and should be used. Several methods have been reported: self-confirmation by photocatalytic reaction products and radical species; selective photodeposition of a noble metal; in situ irradiated x-ray photoelectron spectroscopy (XPS) analysis; surface photovoltage (SPV) technique; time-resolved diffuse reflectance (TDR) spectroscopic analysis [78]. Sometimes, photo-corrosion effects are reduced, which can be a hint for a Z-scheme mechanism (e.g. in composite materials containing CdS) [87].

The investigation of charge transfer processes is essential to describe the photocatalytic activity in a given system and to improve photocatalysts in the future. As mentioned before, heterojunctions and Z-schemes can show undesired charge transfers and backward reactions. We would like to mention that the term S-scheme (step scheme) was also introduced and is mainly synonymously used with direct Z-schemes [88–90]. In this article, the term direct Z-scheme instead of S-scheme is used.

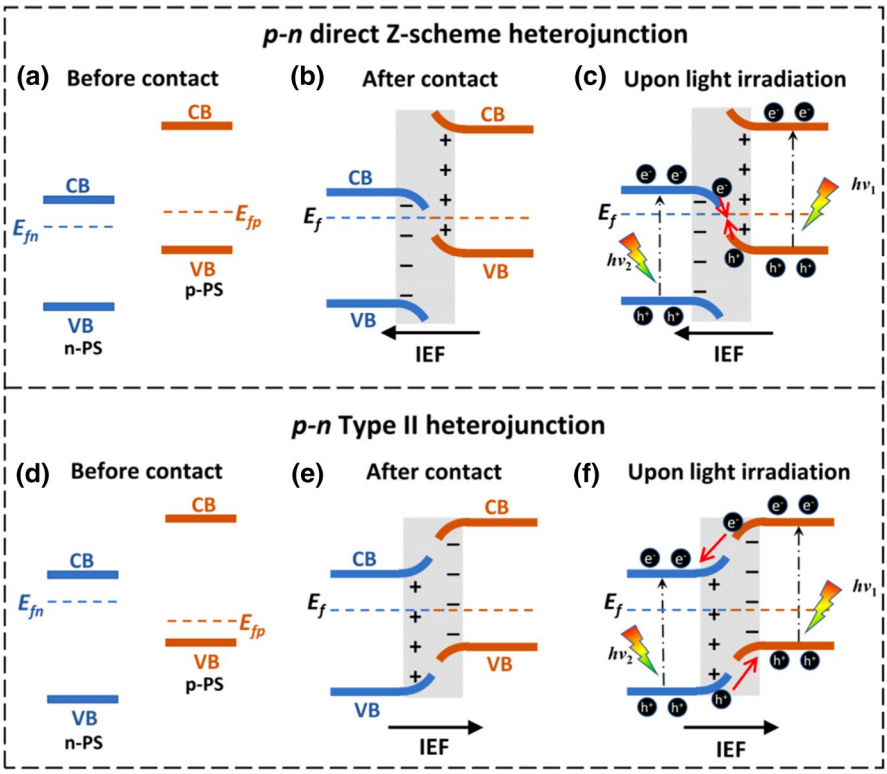

Fig. 9 Schematic of **a**–**c** *p-n* direct Z-scheme heterojunction and **d**–**f** *p-n* type II heterojunction. Reprinted with permission from [82] © 2021 Elsevier

2.3.3.2 Facets and Regulation of Charge Flow Direction Facet design has been discussed many times for various photocatalysts [91, 92]. Direct Z-schemes can also be constructed and improved through facet design. Here, charge flow directions and the recombination of photogenerated charges at interfaces can be regulated [82]. The co-exposed {0 0 1} and {1 0 1} facets of anatase TiO_2, for example, would form a "surface heterojunction" as shown in Fig. 10a. Due to different band structures and band edge positions, photogenerated electrons and holes would transfer to {1 0 1} and {0 0 1} facets, respectively [82, 93].

Anchoring a suitable semiconductor with a smaller work function (higher Fermi level) on the {1 0 0} facet of TiO_2, would lead to the formation of a Z-scheme (Fig. 10b). In contrast, if said semiconductor is deposited on {0 0 1} facets, a type II heterojunction will be formed instead [82]. In 2015, a facet-induced direct Z-scheme between TiO_2 {1 0 1} and g-C_3N_4 was realised by Huang et al. [94].

Jiang et al. used chemical deposition and photodeposition to regulate the electron flow direction in g-C_3N_4/CdS composite materials [95]. In the photodeposition case, a type II heterojunction was constructed because CdS was selectively

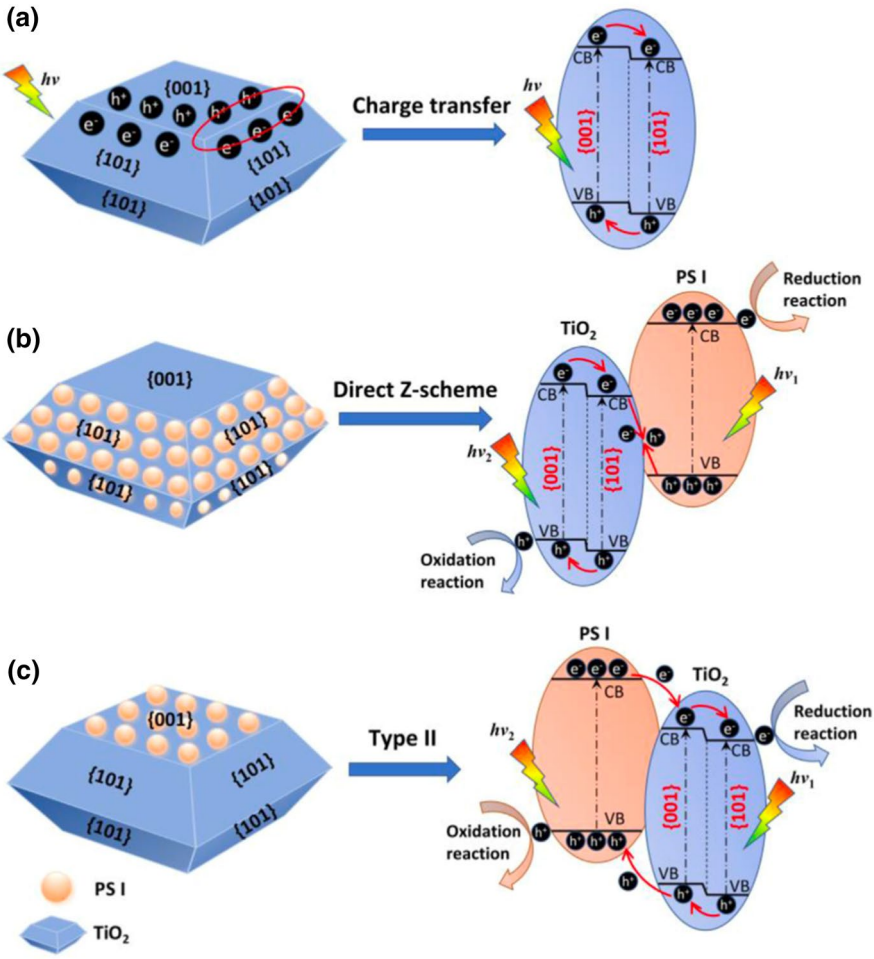

Fig. 10 Charge transfer **a** at the edge of a single TiO_2 nanocrystal, **b** in a direct Z-scheme, and **c** in a type II TiO_2-based heterojunctions induced by facet design. Reprinted with permission from [82] © 2021 Elsevier

deposited at the electron transfer site of g-C_3N_4, resulting in a photogenerated electron transfer from g-C_3N_4 to CdS. Using a chemical deposition technique, CdS was randomly deposited onto g-C_3N_4, which resulted in a Z-scheme charge transfer mechanism [95].

The same group showed in 2019 that deliberate construction of direct Z-scheme photocatalysts was possible by photodeposition [96]. Two routes to construct direct Z-schemes were proposed via photooxidation and photoreduction (Fig. 11).

When g-C_3N_4 was selected as SC-I, Fe_2O_3 as SC-II was selectively deposited on hole-rich sites of g-C_3N_4 through photooxidation (Fig. 11a). When CdS was selected as SC-I, it was selectively deposited on electron rich sites of SC-II (TiO_2) (Fig. 11b)

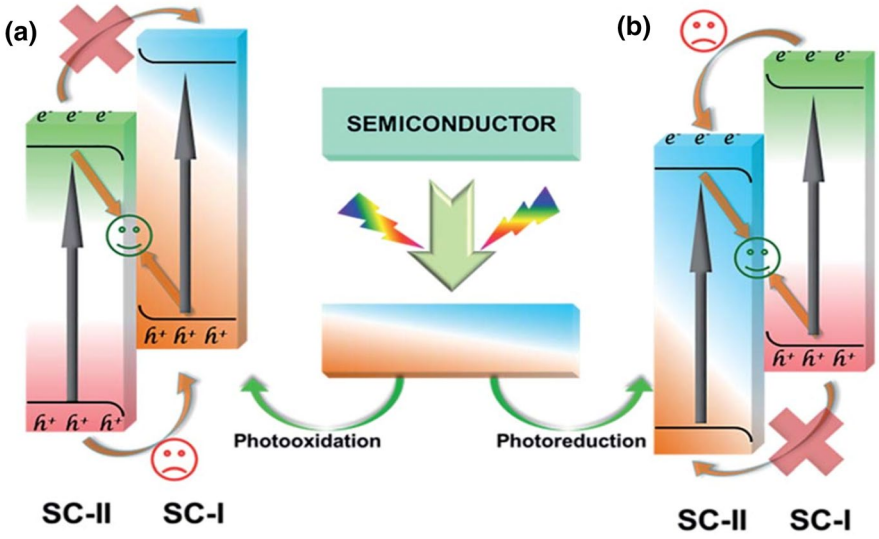

Fig. 11 The construction routes of direct Z-scheme photocatalysts through photodeposition: **a** photodeposition of SC-II (e.g. Fe_2O_3) on SC-I (e.g. g-C_3N_4) through photooxidation; **b** photodeposition of SC-I (e.g. CdS) on SC-II (e.g. TiO_2) through photoreduction (SC = semiconductor). Reprinted with permission from [96] © 2019 Royal Society of Chemistry

[96]. In the future, further investigations might allow to transfer this approach to other materials. A foundation would be extensive investigations of electron- and hole-rich sites and the deliberate construction of these sites for different materials.

2.3.3.3 Dual Direct Z-Schemes Direct Z-schemes can also be built from a combination of three semiconductors. These photocatalysts are usually called "dual Z-schemes" or "ternary Z-schemes" [82]. One advantage of these systems is the better spatial separation of reduction and oxidation reactions which occurs on nonadjacent semiconductors. As a result, recombination rates can be reduced or, in other words, the lifetime of photogenerated charge carriers can be prolonged [82, 97, 98]. Furthermore, a broader light absorption spectrum is achievable [98].

Li et al. divide dual direct Z-schemes into three categories (Fig. 12). According to the shape formed by the position of conduction bands and valence bands relative to each other, these systems are called arrow-down, arrow-up, and cascade dual Z-schemes [82].

In an arrow-down system, the electrons in the CB of PS II combine with holes in the VBs of PS I and PS III. Therefore, the electrons at the CBs of PS I and PS III participate in the reduction reaction while the holes in the VB of PS II participate in the oxidation reaction. In an arrow-up photocatalyst, the band positions are inverted compared to the former described system. Therefore, the reduction takes place at PS II while oxidation takes place at PS I and PS III. In a cascade dual Z-scheme, the electrons in the CB and holes in the VB of PS II combine with the holes in the VB of PS I and electrons in the CB of PS III, respectively [82].

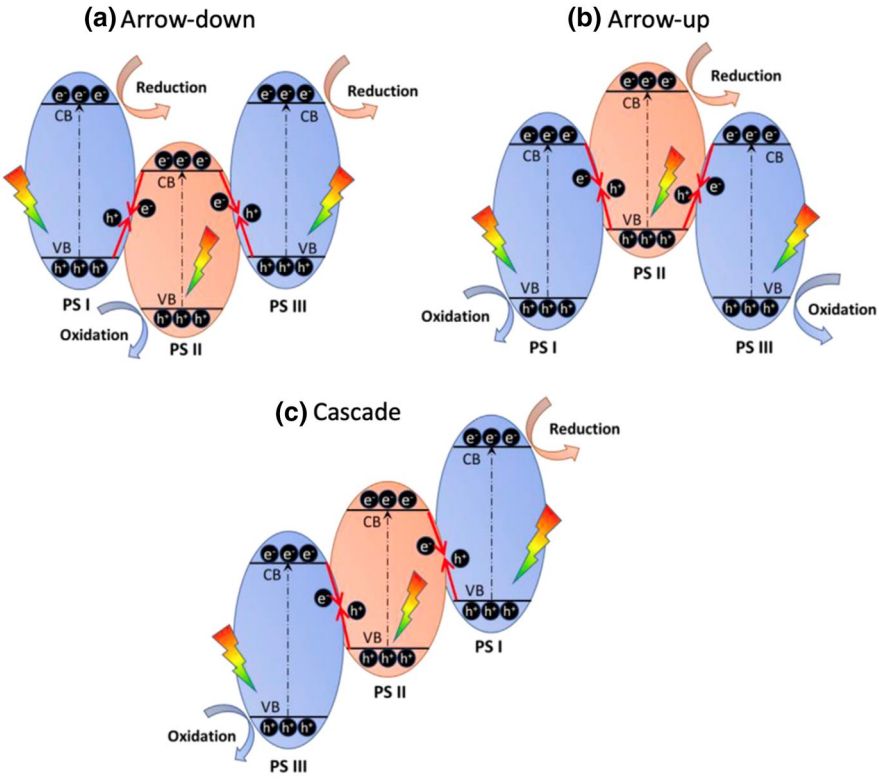

Fig. 12 Band alignments in three types of dual direct Z-schemes: **a** arrow-down, **b** arrow-up, and **c** cascade. Reprinted with permission from [82] © 2021 Elsevier

All three types of dual Z-schemes have been realised in the past few years. An arrow-down dual Z-scheme was demonstrated by Xue et al. in the form of a g-C_3N_4/Bi_2WO_6/AgI combination [99]. An arrow-up dual Z-scheme was reported by Zheng et al. for a Co_3O_4@CoO/g-C_3N_4 combination [100]. In 2019, Wang et al. reported a g-C_3N_4/Zn_2SnO_4N/ZnO cascade dual Z-scheme [97].

Unfortunately, none of these three systems were tested for water splitting or H_2 evolution reactions. In the past 3–4 years, more and more dual direct Z-schemes have been reported aiming at H_2 evolution. Recently, Kumar et al. reported a g-C_3N_4/$Bi_4Ti_3O_{12}$/$Bi_4O_5I_2$ arrow-down dual Z-scheme for photocatalytic antibiotic degradation and H_2 production (Fig. 13) [101].

XPS measurements confirmed that the double Z-scheme mechanism is facilitated or mediated by in-built redox mediators Bi^{5+}/Bi^{3+} and I_3^-/I^- or IO_3^-/I^-. Thus, a complicated dual direct Z-scheme assisted by redox mediators was constructed. Aside from antibiotic degradation, the system was also tested for photocatalytic H_2 evolution in pure water and in solutions containing triethanolamine (TEOA, $6.7{\cdot}10^{-5}$ M) reaching 24.12 mmol g^{-1} h^{-1} and 69 mmol g^{-1} h^{-1}, respectively (Table 1 in the Appendix).

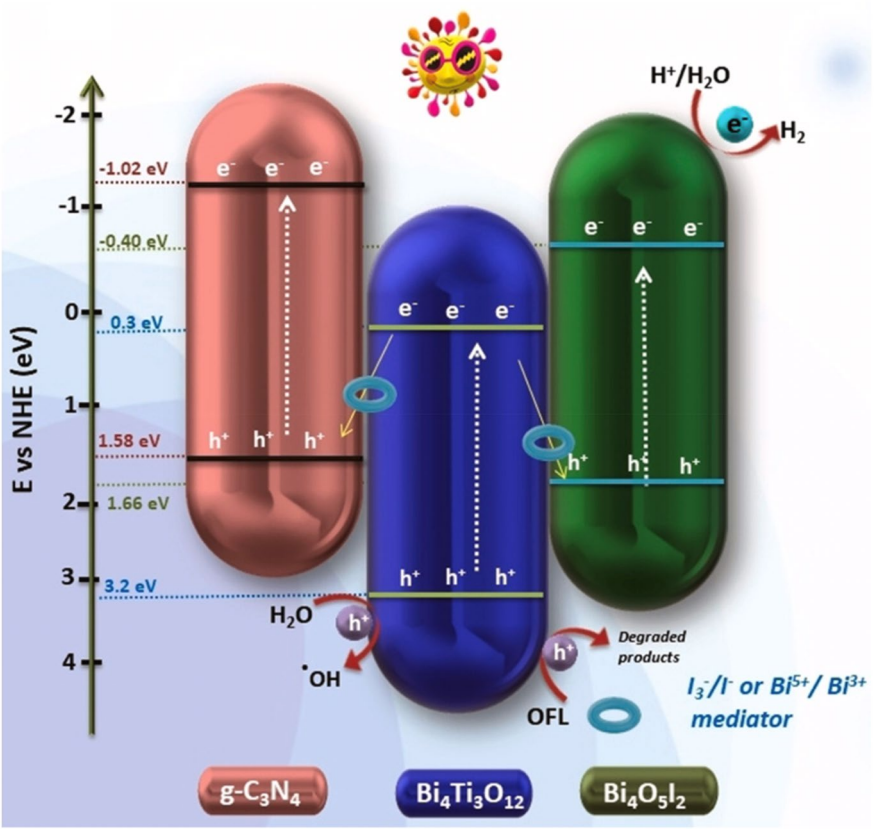

Fig. 13 Photocatalytic mechanism for H_2 evolution and pollutant degradation by dual Z-scheme mechanism. Reprinted with permission from [101] © 2021 Elsevier

Another ternary structure for photocatalytic H_2 evolution reported by Dong et al. used a ZnO/ZnS/g-C_3N_4 cascade dual Z-scheme. The composite displayed specific surface areas of 76.6 m^{-2} g^{-1} and reached a H_2 evolution rate of 0.3 mmol g^{-1} h^{-1} using sacrificial agents (Na_2S and Na_2SO_3) but no co-catalysts [102].

In summary, dual direct Z-schemes are a recent trend and further reports focusing on H_2 evolution reactions and water splitting are expected for the future. Nevertheless, these structures suffer from the limitation of material availability to achieve suitable band alignments [82]. Also, complex synthesis protocols and even more challenging charge transfer analyses are necessary to optimise and understand these systems.

2.3.3.4 Z-Schemes with MOFs and COFs Metal organic frameworks (MOFs) are one-, two-, or three-dimensional coordination networks consisting of metal ions/clusters linked together by organic linker molecules. MOFs have received growing attention in the construction of direct Z-schemes. Advantages like tuneable

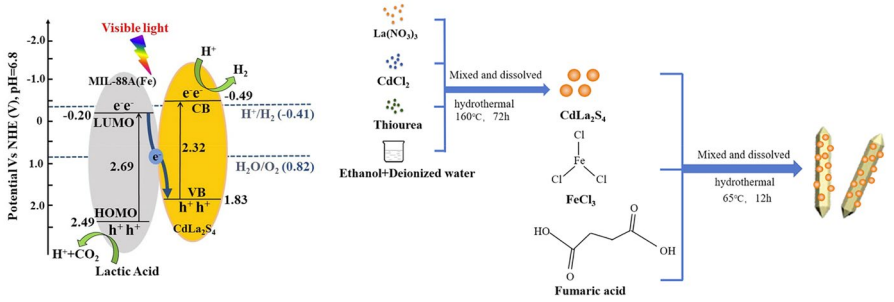

Fig. 14 Band alignments in the $CdLa_2S_4$/MIL-88A(Fe) Z-scheme (left) and synthesis process of the composite (right). Reprinted with permission from [104] © 2019 Elsevier

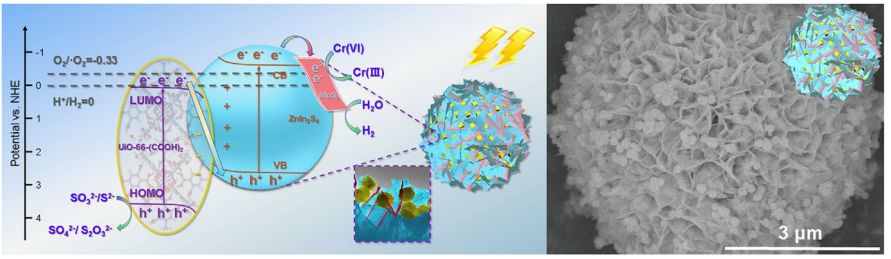

Fig. 15 Proposed photocatalytic Z-scheme mechanism (left) and field-emission scanning electron microscope (FESEM) image of the UiO-66-$(COOH)_2$/$ZnIn_2S_4$ (yellow/blue) photocatalyst decorated with MoS_2 co-catalyst (red) (right). Reprinted with permission from [106] © 2019 Elsevier

composition and light-harvesting property, high surface areas, and controllable pore sizes make MOFs attractive in applications of photocatalysis [82, 103]. The visible light photocatalytic performance of pure MOFs is quite poor. However, in direct Z-schemes significant improvements have been reported [82, 104–106]. Various morphologies are easily achievable, which enables the use of 3D, 2D, and 1D structures in direct Z-schemes. Chen et al. constructed a direct Z-scheme by anchoring $CdLa_2S_4$ nanoparticles on 1D MIL-88A(Fe) micro-rods (Fig. 14). The nanocomposite obtained high H_2 evolution rates of up to 7.678 mmol g^{-1} h^{-1} using a 20 wt% content of MIL-88A(Fe). Moreover, the $CdLa_2S_4$/MIL-88A(Fe) composite exhibited high durability during the photocatalytic H_2 evolution [104].

The high photocatalytic activity mainly contributed to the formed Z-scheme structure [104].

In 2019, a 3D hierarchical structure of a UiO-66-$(COOH)_2$/$ZnIn_2S_4$ Z-scheme was reported [106]. Here, UiO-66-$(COOH)_2$ nanoparticles were decorated in the interweaving petal nanosheets of $ZnIn_2S_4$ microspheres, while co-catalyst MoS_2 nanosheets were folded at the edge of these interweaving petals as shown in Fig. 15.

The optimised photocatalyst showed high H_2 evolution rates of 18.794 mmol g^{-1} h^{-1}, which was about 15.3 times higher than the H_2 evolution rate of pure $ZnIn_2S_4$.

Overall, only a small group of MOFs are suitable for H_2 evolving or water splitting photocatalytic applications since most MOFs are known to become unstable if exposed to moisture/water. However, > 40 MOFs are known to show enhanced water stability (amongst others MIL-100, MIL-101, UiO-66, Zn-DMOF, DUT-67) [107]. Considering possible morphologies and composite materials containing MOFs, there still seems to be potential for stable and low-cost direct Z-schemes in the future.

Covalent organic frameworks (COFs) are crystalline covalent polymers with a high surface area. These porous materials with tuneable topology and functionalities have gathered significant interest among researchers in the field of photocatalysis [108, 109]. The moderate band gap and the presence of extended π-conjugated electronic networks enable visible-light responsive ability and possibilities for bandgap engineering. Therefore, COFs and COF-linked hybrid materials are used as photocatalysts for H_2 production. Due to the stability of covalent bonds compared to coordinate bonds in MOFs, COFs are known to exhibit high stability in various solvents even under harsh acidic, basic, oxidative, or reductive conditions. However, a majority of reported photocatalytic COFs are based on imine, hydrazone, or azine linkages and are considered unstable for extended photocatalysis in water [108]. Currently, only a few COF materials have been investigated for photocatalytic H_2 evolution or water splitting. Nonetheless, there has been considerable progress regarding stability and photocatalytic activity in the past few years. One example is sulfone-containing COFs reported in 2018 by Wang et al. [110]. These covalent organic frameworks are based on a benzobis(benzothiophene sulfone) moiety and are stable for at least 50 h in water under visible light irradiation. Using ascorbic acid (0.1 M) as a sacrificial electron donor and Pt as a co-catalyst (8 wt%), H_2 evolution rates of up to 10.1 mmol g^{-1} h^{-1} were obtained (300 W Xe light source). Without the addition of co-catalyst, still significant rates of up to 1.32 mmol g^{-1} h^{-1} were reported [110]. Their internal pore structure could be decorated with nanoparticles/quantum dots, making these COFs a platform for developing hybrid photocatalysts.

In 2020, a COF-based noble-metal-free Z-scheme (TpPa-2-COF/α-Fe_2O_3) was reported for the first time [111]. The transfer of photogenerated electrons from the CB of α-Fe_2O_3 to the VB of the TpPa-2-COF was confirmed, and the effectiveness of the Z-scheme structure attributed to the tight integration between the metal oxide and the COF. As illustrated in Fig. 16, the hybrid material was synthesised by a simple one-pot synthesis using α-Fe_2O_3, 1,3,5-triformylphloroglucinol and 2,5-dimethyl-*p*-phenylenediamine.

The co-catalyst free Z-scheme showed H_2 evolution rates of up to 3.77 mmol g^{-1} h^{-1}, which is about 53 times higher than that of the parent TpPa-2-COF und the same conditions and even better than that with a Pt (2 wt%) co-catalyst [111].

Compared to MOFs, COFs are still "young", but their cheap synthesis, tuneable pores, and other characteristics like visible-light absorption make them attractive for the application as photocatalysts. Hybrids with metal-oxides have already

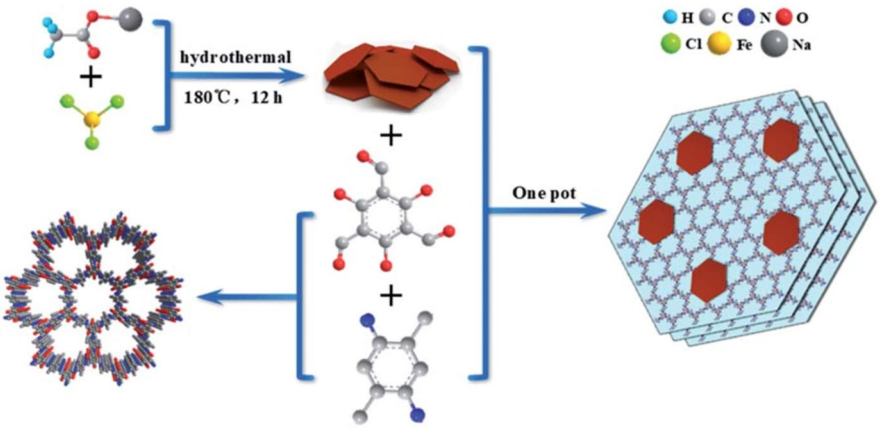

Fig. 16 Schematic illustration of the synthesis of an α-Fe_2O_3/TpPa-2-COF hybrid material. Reprinted with permission from [111] © 2020 Royal Society of Chemistry

demonstrated significant performance improvements [82]. Hybrid materials based on already optimised COFs from recent publications might lead to even higher photocatalytic activity.

2.3.3.5 Coupling Surface Plasmon Resonance (SPR) Effect into Direct Z-Scheme Systems Another strategy to improve photocatalytic activity is coupling surface plasmon resonance (SPR) into direct Z-schemes. SPR is the collective oscillation of electrons that are in resonance with the oscillating electric field of incident light [112]. Resonances near the visible or near IR range can enhance the light absorption ability of the photocatalytic system. In addition, SPR-induced hot plasmon electrons or SPR-enhanced localised electromagnetic fields can boost the charge separation near the interfaces between the SPR material and the semiconductor [82, 113, 114]. Well-known materials are noble metals (Ag and Au) and heavily doped semiconductors (H_xWO_3, $W_{18}O_{49}$ and BiO_{2-x}) [82].

Among these materials, noble metals are most commonly used for application in photocatalysis. The Schottky junction supplies an internal electric field between the noble metal and the semiconductor, which improves the interfacial charge transfer. Localised surface plasmon resonances (LSPR) can enhance solar light absorption. Both features can lead to significant enhancement of the photoreactivity [82, 113]. This was described, for example, in TiO_2/Au/WO_3 or TiO_2/Ag/Cu_2O Z-schemes for H_2 generation [115, 116]. Other examples or Z-scheme couples with LSPR for photocatalytic H_2 generation include TiO_2/Pt/WO_3 [117], TiO_2/Au/CdS [118], C_3N_4/Au/TiO_2 [119], C_3N_4/Ag/$NiTiO_3$ [120], C_3N_4/Ag/SnS_2

[121], $SrTiO_3/C_3N_4/Ag/Fe_3O_4$ [122], and $C_3N_4/Ag/CdS$ [123]. In contrast, for a $Ag/C_3N_4/TiO_2$ system, a SPR-enhanced heterojunction was reported, with Ag not acting as electron mediator simultaneously [124].

Xie et al. combined modified C_3N_4 ($NCN\text{-}CN_x$) with gold nanoparticles and $CuInS_2$ to achieve photocatalytic hydrogen evolution from water/triethanolamine, reaching 4.28 mmol h^{-1} g^{-1} at wavelengths > 550 nm [125]. Interestingly, surface photovoltage spectroscopy was additionally used to confirm the SPR effect and the synergistic effects of SPR and Z-scheme mechanism.

Modulating the stoichiometric ratio of certain semiconductors is also used to improve light absorption abilities since it can increase the free-charge density and lead to LSPR arising from collective oscillations of the excess free-charges on the semiconductor surface [126]. Blue $W_{18}O_{49}$ is a nonstoichiometric tungsten oxide with a bandgap of 3.0 eV and exhibits LSPR absorption in both the vis and NIR region because of abundant oxygen vacancies on its surface. Zhang et al. used this material to synthesise a $g\text{-}C_3N_4/W_{18}O_{49}$ plasmonic Z-scheme photocatalyst, which could harvest photon energies spanning from the UV to the near IR region [126]. A wavelength range of 450–900 nm electrons near the Fermi level of $W_{18}O_{49}$ reached the high-energy surface plasmon state and became plasmonic "hot electrons", which then could partly transfer to the conduction band of $g\text{-}C_3N_4$. The system reached H_2 evolution rates of up to 3.04 mmol g^{-1} h^{-1} when triethanolamine (15 vol%) was used as sacrificial agent.

Although considerable progress has been made in plasmonic metal-based and nonmetal-based photocatalysts, challenges remain such as low utilisation of hot carriers, uncovered mechanisms of hot carrier-driven reactions, and the exploration of novel (nonmetallic) plasmonic materials. Therefore, the full potential of plasmonic materials for efficient photocatalytic systems is yet to be realised [127].

2.3.3.6 Upconversion Photoluminescence (UCPL) Materials in Z-Schemes Besides the (L)SPR materials, most direct Z-scheme photocatalysts can only utilise the light energy in the UV and visible region. These materials' inability to utilise light from the near IR (NIR) region is an impediment in the progressive photocatalysis research since NIR light constitutes the maximum portion of solar energy (approximately 50%) [128]. Therefore, efficient full-spectrum-activated (UV–Vis–NIR) photocatalysts have gained a lot of attention. An attractive strategy is to integrate non-linear UCPL materials in direct Z-scheme systems [82, 129].

UCPL materials exhibit a multi-photon-assisted anti-Stokes excitation mechanism, which enables the conversion of low energy (NIR) photons into radiation of UV and visible light [130]. Rare-earth-based lanthanide-doped materials, such as Yb^{3+}- and Er^{3+}-doped $NaYF_4$, are popular UCPL substances [82]. Unfortunately, rare earth-doped upconversion materials generally suffer from low upconversion efficiency due to small absorption cross sections and low energy transfer efficiencies [131]. In doped $NaYF_4$, the upconversion characteristics entirely depend on

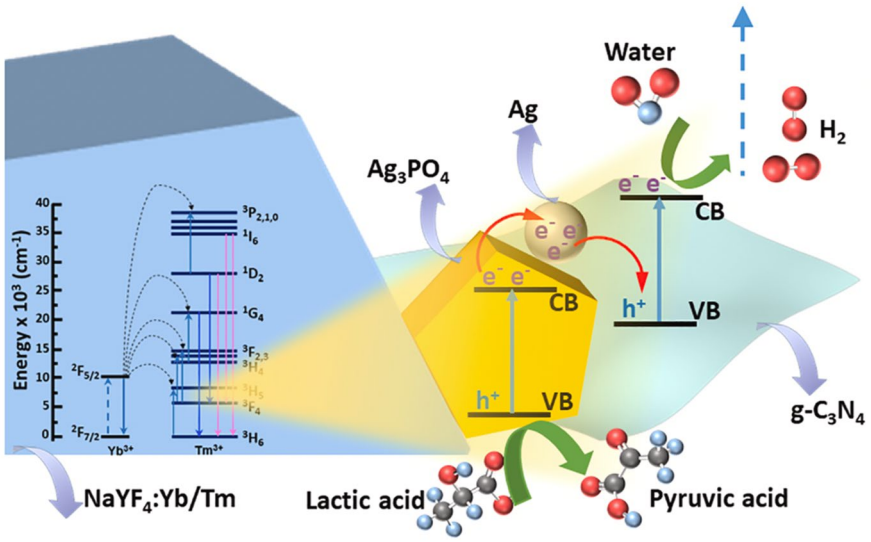

Fig. 17 Schematic representation of the photocatalytic H_2 evolution mechanism of g-C_3N_4/Ag_3PO_4 Z-scheme photocatalyst under the sunlight illumination using Yb/Tm-doped $NaYF_4$ as an UCPL material and lactic acid as a sacrificial agent. Reprinted with permission from [128] © 2021 Elsevier

the selection of dopants [132]. Yb/Tm-doped $NaYF_4$, for example, exhibits several UV–visible upconversion emission peaks that fall under the absorption range of semiconductor photocatalysts. Recently, this material has been used by Murali et al. for a NIR-activated g-C_3N_4/Ag_3PO_4 Z-scheme [128]. The mechanism behind the NIR-light utilised photocatalytic H_2 production is shown in Fig. 17.

The NIR photons in solar irradiation excite Yb^{3+} ions in the $NaYF_4$ host from the ground state ($^2F_{7/2}$) to the excited state ($^2F_{5/2}$). These excited Yb^{3+} ions act as sensitisers and populate higher energy levels of Tm^{3+} ions. Non-radiative relaxation of Tm^{3+} ions populates several other of its energy levels. The energy is then transferred to the g-C_3N_4/Ag_3PO_4 via Förster resonance energy transfer (FRET). The absorption of additional energy by the UV–visible g-C_3N_4/Ag_3PO_4 Z-scheme spurs the number of free charges. In this particular system, Ag^0 comprised in Ag_3PO_4 additionally acts as a channel between both semiconductors [128].

Yb/Tm-doped $NaYF_4$/Ag_3PO_4 was also combined with black phosphorus for another Z-scheme/UCPL heterostructure [133]. Interestingly, a laser source (980 nm) was used as light source to prove the NIR upconversion; 0.146 mmol g^{-1} h^{-1} H_2 evolution from aqueous glycerol solution (50 vol%) could be achieved, with 0.077% apparent quantum efficiency at 980 nm.

TiO_2 was also used in combination with other semiconductors and UCPL materials for photocatalytic H_2 evolution. Together with g-C_3N_4 and carbon quantum dots, photocatalytic water splitting was achieved in a 2:1 ratio at a maximum H_2 evolution rate of

6.497 μmol h^{-1} g^{-1} under 300 W Xe illumination (> 400 nm) [134]. Therein, the carbon quantum dots are supposed to have a dual function as upconversion material and catalyst for H_2O_2 decomposition, therefore facilitating oxygen evolution and water splitting.

Iron-doped TiO_2 combined with vanadium-doped Ta_2O_5 and Er^{3+}:$YAlO_3$ as UCPL were applied for photocatalytic H_2 generation from aqueous methanol solutions, including decoration with gold nanoparticles [135]. Er^{3+}:$YAlO_3$ was used as UCPL agent from visible-light to ultraviolet-light to be able to excite the wide band gap oxides with visible light, and a Z-scheme was established by the dopants resulting in a TiO_2-Fe^{3+}/V^{5+}-Ta_2O_5 redox cycle system. By irradiation with a 300-W Xe lamp and a cut-off filter, H_2 evolution activity of approximately 32 μmol h^{-1} g^{-1} was shown in visible light.

These examples show that the combination of UCPL materials and Z-schemes or heterojunctions is another promising method to enhance the sunlight absorption of semiconductor photocatalyst systems for H_2 generation and water splitting. More efforts are however needed to optimize the FRET to the semiconductors to improve the overall solar-to-H_2 efficiency.

2.3.3.7 2D/2D Z-Schemes Among the various developed photocatalysts, 2D materials are receiving increasing attention because of their unique physical and chemical properties [136]. Compared with bulk photocatalysts, 2D photocatalysts have a higher specific surface area due to their planar structure and ultralow thickness. Additionally, more surface atoms can provide more adsorption and active sites for photocatalytic reactions [78]. Constructing 2D/2D Z-scheme heterojunctions can combine the respective advantages of 2D materials and Z-scheme systems.

Zhu et al. fabricated a 2D/2D BP/$BiVO_4$ Z-scheme (BP = black phosphorus) and realised overall water splitting [137, 138]. Thin BP and $BiVO_4$ were hybridised by electrostatic interactions. In both photocatalytic H_2 and O_2 production processes, the 2D/2D Z-scheme exhibited better photocatalytic activities than BP and $BiVO_4$ alone. H_2 and O_2 production rates of 0.16 mmol g^{-1} h^{-1} and 0.102 mmol g^{-1} h^{-1}, respectively, and an apparent quantum efficiency of 0.89% were realised [137, 138].

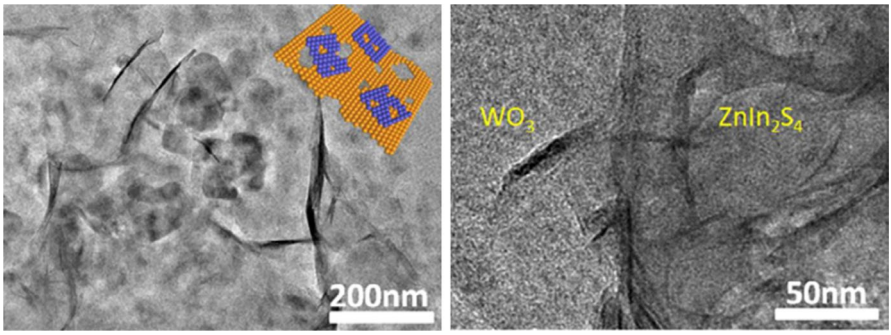

Fig. 18 TEM images of the 2D/2D $ZnIn_2S_4$/WO_3(10 wt%) Z-scheme. Reprinted with permission from [139] © 2019 Elsevier

Li et al. prepared a Janus sulphur vacancy-rich $ZnIn_2S_4/WO_3$ Z-scheme [139]. The Janus bilayer was fabricated via electrostatic self-assembly by adding WO_3 nanosheets into the precursor of $ZnIn_2S_4$. TEM images of the 2D/2D $ZnIn_2S_4/WO_3$ (10 wt%) composite are shown in Fig. 18.

Vacancy-rich $ZnIn_2S_4$ was chosen because the sulphur vacancies significantly promoted H_2 production due to optimised charge separation and light utilisation. The Z-scheme photocatalyst obtained H_2 evolution rates of up to 7.81 mmol g^{-1} h^{-1}, which was about 20.8 and 1.69 times higher than those of $ZnIn_2S_4$ and Pt-$ZnIn_2S_4$. In addition, the loading of NiS quantum dots as co-catalyst could further improve the photocatalytic H_2 production, which reached 11.09 mmol g^{-1} h^{-1}. This is the highest photocatalytic activity toward visible-light-driven H_2 evolution among the family of $ZnIn_2S_4$ materials reported so far.

In addition to the previous examples, 2D/2D Z-schemes were also reported for g-C_3N_4/Fe_2O_3 [140], g-C_3N_4/WO_3 [141], g-$C_3N_4/BiVO_4$ [142], $Zn_{0.67}Cd_{0.33}S/Cu_2S$ [143], $Zn_xCd_{1-x}S/ZnO$ [144], g-$C_3N_4/La_2Ti_2O_7$ [145], and several other composite materials. Some of these 2D/2D Z-schemes are listed in Table 1 in the appendix.

More than 3000 papers on 2D/2D Z-scheme photocatalyst have been published, more than 700 of them in 2021 alone (data from SciFinder^n). Research on 2D/2D composites is therefore a major trend in the field of Z-scheme photocatalysis, which cannot be fully covered in this review. Interested readers are referred to other excellent reviews [78, 146–149].

3 Comparison, Trends, and Conclusion

Considering heterojunctions and Z-schemes reported in the last 5 years, high H_2 evolution rates were achieved, for example, for $CdLa_2S_4$/MIL-88(Fe) (7.678 mmol g^{-1} h^{-1}) [104], g-C_3N_4/CdS (10.89 mmol g^{-1} h^{-1}) [150], g-C_3N_4/Ag_3PO_4 (23.56 mmol g^{-1} h^{-1}) [128], $CoTiO_3$/UiO-66 (26.545 mmol g^{-1} h^{-1}) [151], CdS/(Au/)TiO_2 (47.6 mmol g^{-1} h^{-1}) [118], CdS/$BiVO_4$ (23 and 57 mmol g ^{1} h^{-1}) [87, 152], g-$C_3N_4/Bi_4Ti_3O_{12}/Bi_4O_5I_2$ (69 mmol g^{-1} h^{-1}) [101], CdS/ZnO (98.82 mmol g^{-1} h^{-1}) [153], and several other photocatalytic systems (Table 1 in the Appendix).

Unfortunately, these values are not comparable because of differences in measurement setups, light sources, intensity, filters, co-catalysts, and several other factors. H_2 evolution rates from > 50 publications have been evaluated and are listed in Table 1 in the appendix. Nevertheless, we hope that the readers of this article find it useful to compare some parameters used for hydrogen production in literature recently. Some of the production rates are very high and could also be a result of normalising the given rate in the publication to the used catalyst mass. Furthermore, high rates were often reported when low catalyst weights (<20 mg) were used [139, 152, 153]. This may indicate that rather small setups were used or that weighing errors can lead to incorrect production rates. In some cases, no production rates were given, and we had to estimate hydrogen production rates from graphical depictions [128, 154, 155]. It is

moreover well known that in photocatalysis the observed rates should not be normalized to the photocatalyst mass because of scattering and shadowing effects leading to non-linear correlation of photocatalyst mass and activity [156].

Therefore, no particular heterojunction or Z-scheme can be seen as superior based on stated H_2 evolution rates. However, composite materials containing CdS, $BiVO_4$, or g-C_3N_4 often show high photocatalytic activity when combined with a suitable second semiconductor. Furthermore, new strategies like 2D/2D Z-schemes, the use of upconversion photoluminescent materials, or deliberate syntheses led to enhanced H_2 production rates.

A benchmark was set in 2016 by Wang et al. who presented a photocatalyst sheet with a Z-scheme charge carrier transfer based on La- and Rh-codoped $SrTiO_3$ and Mo-doped $BiVO_4$ embedded into a gold layer [157]. A solar-to-H_2 energy conversion of 1.1% and an apparent quantum yield of > 30% for pure water splitting was reported. Unfortunately, only in one third of the reviewed publications were apparent quantum yields stated. Values for solar-to-H_2 energy conversion are also only given for a few cases.

Since different sacrificial agents (MeOH, TEOA, lactic acid, NaS, Na_2SO_3, etc.) and different concentrations of sacrificial agents were used to enhance H_2 production rates, this caused additional problems for good comparability. Here, the need for sacrificial agents is viable for mechanistic studies and should be avoided when the aim to maximise hydrogen production is discussed.

In 2015, Horst Kisch discussed that apparent quantum yields cannot be compared in a quantitative way. Clear standards are needed to make apparent quantum yields and evolution rates to some extent comparable. Kisch proposed that *optimal rates* should be measured in one unique photoreactor at a given lamp intensity [158]. Common standards, including a standard photoreactor, are needed in the field of photocatalysis and will be inevitable at some point. These standards will not be perfectly suitable for every photocatalyst, but standardised measurements could establish a better comparability.

In terms of materials, in the past 5 years a clear trend toward direct Z-schemes has been recognisable. Heterojunctions have been discussed extensively for decades and are still prominent in photocatalysis research, but nowadays more attention is paid to Z-schemes because of their stronger redox capabilities. Z-schemes are now in the third generation, called direct Z-schemes, and have lost several of the drawbacks of their predecessors (redox mediated Z-schemes and all-solid-state Z-schemes) such as backward reactions and light-shielding problems.

Various new heterojunctions and Z-schemes have been reported in the last years. Overall, a number of trends can be identified that also leave room for new approaches and ideas:

Nanoparticles, nanosheets, and other 0D, 1D, 2D, or 3D structures are commonly used in all kinds of photocatalysts and in (direct) Z-schemes. However, mesoporous Z-schemes are rarely reported. In some of these reports, the mesoporous structure is not even discussed or further investigated [159, 160]. High specific surface areas,

enhanced diffusion of reactants, and improved charge carrier transfer (for example because of an "antenna mechanism" [39]) would make mesoporous Z-schemes promising photocatalysts. Obviously, one mesoporous semiconductor (PS I or PS II) would not be capable of being in intimate contact with a bulk material since the contact area would be significantly reduced because of the pores. Two-dimensional materials such as nanosheets might even block pores, which would take away the advantages of a mesoporous semiconductor. Therefore, careful material design of macroporous/mesoporous heterojunctions might be a way to partially maintain a porous structure and achieve sufficient contact between two semiconductors. Another approach would be core-shell Z-schemes with a porous or incomplete outer shell. This might be a promising strategy, especially for semiconductors in the core that are prone to corrosion or other effects.

The 2D/2D type Z-schemes are probably the most interesting trend in Z-scheme photocatalysis research. Nonetheless, their synthesis is challenging, and large-scale synthesis protocols are lacking so far. Furthermore, 2D structures are mostly reserved to layered semiconductors. Effective synthetic methods need to be developed to produce 2D photocatalysts from non-layered semiconductors, as has been done for $SrTiO_3$ for example [161].

In general, intimate contact seems to be crucial for Z-scheme charge carrier transport. Typical mechanical/physical methods, such as ball-milling, grinding, or simple mixing of the materials, are frequently used. However, composites assembled by these methods have no intimate interface and both semiconductors are easily detached from each other. Strong interaction is favoured by in-situ growth strategies, hydrothermal and solvothermal treatment, solid-state synthesis, ion-exchange, and electrospinning [77].

Interestingly, chemical deposition of a semiconductor was used to deliberately construct Z-schemes (g-C_3N_4/CdS) while photodeposition led to the formation of a type II heterojunction [95]. It is worth mentioning that the type II heterojunction exhibited higher photocatalytic activity. Deliberate construction of Z-schemes is also possible using photooxidation and photoreduction [96]. These techniques might be applicable to other semiconductors such as CeO_2 in case of photooxidation and a variety of metal sulphides for photoreduction.

The field of photocatalysis has experienced a revival of certain materials. Doped $SrTiO_3$, for example, was intensively studied for many years and was used in the probably most prominent example for a Z-scheme ($SrTiO_3$:La,Rh/Au/$BiVO_4$:Mo) [157]. The question therefore arises as to the extent to which other semiconductors could be optimised for improved charge carrier transfer in Z-schemes and heterojunctions. Oxygen/sulphur vacancies and mid gap states have been used in several Z-schemes [58, 145, 162–164]. Intrinsic defects and doping strategies could be applied to other semiconductors to further improve charge carrier transport in direct Z-schemes.

Black phosphorous is another semiconductor that research has focused on recently. For example, a black/red phosphorus multiphase heterojunction has been

prepared and tested for water splitting [154, 155]. Furthermore, supported black phosphorus nanosheets as H_2-evolving photocatalyst achieved 5.4% energy conversion efficiency, demonstrating the potential of black phosphorus-based materials [165].

Apart from improving existing Z-schemes by doping and new combinations of known semiconductors, new material classes have been introduced. Metal organic frameworks (MOFs) and more recently covalent organic frameworks (COFs) have been used in Z-scheme photocatalysts [104–106, 111, 151]. Other continuing trends are localised surface plasmon resonances (LSPR) and upconversion photoluminescent (UCPL) materials to improve the light absorption of photocatalysts in the visible and near IR range.

In summary, heterojunction and (direct) Z-scheme photocatalysts with multiple semiconductor combinations are still highly investigated in photocatalysis research for hydrogen generation, with different materials strategies addressing varying issues including light absorption over broad wavelength range and charge carrier separation. New types of materials classes such as MOFs and COF and 2D materials are included in heterojunctions and Z-schemes more frequently. Both remain extremely promising material designs and present unique advantages over single material photocatalysts for hydrogen generation; the recent trends and developments have been presented in this work. Although promising approaches such as the application of LSPR and UCPL materials as well as new material combinations, new syntheses, sophisticated morphologies, and improved doping strategies will inevitably make photocatalytic systems more complex, the increase in complexity is and will be the result of knowledge-based improvements [6] developing new and better absorber combinations for hydrogen generation, which might allow, one day, the large-scale production of green H_2 from photocatalytic water splitting.

Appendix

Table 1 Recent heterojunction (red) and Z-scheme (blue) photocatalytic systems for H_2 evolution (light colour) or water splitting (dark colour), respectively

Catalyst: Z-Scheme (PS I/PS II); Heterojunction (higher CB/lower CB)	Band-gap (eV/eV)	Catalyst amount	Co-catalyst, mass ratio (wt. %)	Synthesis of the composite material	Light source	Yield/ production rate	Sacrificial agents, volume	Apparent quantum efficiency (AQE)	Comment	Ref./ year
BCN/TiO_2	2.72/3.21	50 mg	Pt, -	ball milling	300 W Xe lamp (λ > 420 nm)	0.003 mmol h^{-1} H_2 → 0.06 mmol g^{-1} h^{-1} H_2	20 vol.% triethanolamine (TEOA), 100 ml	-	all-solid state Z-scheme with a O_2 vacancy layer as contact interface; no details of Pt amounts as co-catalyst given	[162] 2018
CdLa$_2$S$_4$/MIL-88(Fe)	2.32/2.69	50 mg	-	hydrothermal	300 W Xe lamp (λ > 420 nm)	7.678 mmol g^{-1} h^{-1} H_2	10 vol.% ethanedioic acid, 100 ml	10.3 % at 420 nm	Z-scheme containing a metal organic framework (MOF); H_2 evolution rate almost 8 times higher than that of pristine CdLa$_2$S$_4$	[104] 2020
CdS/$Bi_{20}TiO_{32}$/$Bi_4Ti_3O_{12}$	2.2/2.42/2.96	100 mg	-	combustion, hydrothermal	250 W Xe lamp (λ > 400 nm)	1.890 mmol g^{-1} h^{-1} H_2	MeOH, 80 ml	-	type I bridged coupled Z-scheme electron migration	[68] 2022
CdS/$BiVO_4$	2.2/2.5	10 mg	Pt, 0.5	precipitation	300 W Xe lamp (λ > 420 nm)	CdS: 0.11 mmol h^{-1} H_2 CdS–$BiVO_4$: 0.57 mmol h^{-1} H_2 → 57 mmol g^{-1} h^{-1} H_2	25 vol.% MeOH, 50 ml	20.6 % at 420 nm	CdS nanoparticles on $BiVO_4$ nanosheets	[152] 2017
CdS/$BiVO_4$	2.25/2.4	50 mg	Pt, 2	hydrothermal	320 W Xe lamp (λ > 420 nm)	CdS: 0.034 mmol h^{-1} H_2 CdS/$BiVO_4$: 1.153 mmol h^{-1} → 23 mmol g^{-1} h^{-1} H_2	20 vol.% lactic acid/ 1 M Na_2SO_3, 200 ml	-	CdS nanoparticles on $BiVO_4$ nanowires, 70 % performance fading over 10 hours in lactic acid solution	[87] 2017
CdS/ZnO	2.28/3.0	100 mg	-	chemical deposition	300 W Xe lamp	with increased oxygen vacancies: 1.329 mmol g^{-1} h^{-1} H_2 without increased oxygen vacancies: 0.584 mmol g^{-1} h^{-1} H_2	0.1 M Na_2S and 0.1 M Na_2SO_3, 270 ml	with increased oxygen vacancies: 19.01 % at 380 nm without increased oxygen vacancies: 12.94 % at 380 nm	oxygen vacancies promote the direct Z-scheme transfer process	[163] 2017
CdS/(Au)/TiO_2	2.4/3.26	50 mg	- (Au)	stirring	300 W Xe lamp	47.6 mmol g^{-1} h^{-1} H_2	0.25 M Na_2S and 0.35 M Na_2SO_3, 100 ml	9.83 % at 450 nm	SPR effect and internal electron transfer ability depending on the size of Au nanoparticles	[118] 2021
CdS/TiO_2	2.4/3.2	50 mg	-	ionic layer adsorption and reaction (SILAR)	350 W Xe lamp	0.0514 mmol h^{-1} H_2 → 1.028 mmol g^{-1} h^{-1} H_2	25 vol.% MeOH, 80 ml	-	CdS nanoparticles on TiO_2 microspheres	[166] 2017
CdS/WS_2	2.17/1.79	50 mg	- (CoP, WS_2)	hydrothermal	300 W Xe lamp (λ > 420 nm)	0.0092 mmol h^{-1} H_2	-, 100 ml H_2O	1.34 % at 420 nm	*p-n*-*n* tandem heterojunction (decorated with CoP); no oxidation product confirmed in pure water	[66] 2019
CdS/ZnO	2.4/3.2	10 mg	Pt/PdS, -	atomic layer deposition (ALD)	225 W Xe lamp (320 nm < λ < 780 nm)	71.39 mmol g^{-1} h^{-1} for Pt co-catalyst 98.82 mmol g^{-1} h^{-1} for PdS co-catalyst 11.36 mmol g^{-1} h^{-1} without co-catalyst	0.35 M Na_2S and 0.25 M Na_2SO_3, 100 ml	-	CdS@ZnO core-shell structure, extremely high H_2 production rates	[153] 2017
Co_9S_8/CdS	0.89/2.4	20 mg	-	solvothermal	300 W Xe lamp (AM 1.5)	1.06 mmol g^{-1} h^{-1} H_2	Na_2S and Na_2SO_3 (unknown conc.)	-	hollow structure might allow multiple reflections	[167, 168] 2017
CoTiO$_3$/UiO-66-NH_2	2.36/2.67	20 mg	-	hydrothermal	300 W Xe lamp (λ > 420 nm)	0.5309 mmol h^{-1} H_2 → 26.545 mmol g^{-1} h^{-1} H_2	10 vol.% MeOH, 20 ml	-	*p-n* heterojunction containing a metal organic framework (MOF); unclear H_2 evolution rate	[151] 2020
CuInS$_2$/g-C_3N_4	1.75/2.75	50 mg	-	hydrothermal	300 W Xe lamp (λ > 420 nm)	1.290 mmol g^{-1} h^{-1} H_2	10 vol.% TEOA and 0.25 M Na_2S and 0.2 M Na_2SO_3, 10 ml	-	Z-scheme verification via deposition of Pt on electron rich sites	[169] 2017
Cu$_3$P/Bi_2WO_6	1.6/2.8	100 mg	-	ball-milling	150 W Xe lamp	0.0047 mmol g^{-1} h^{-1} H_2 0.0023 mmol g^{-1} h^{-1} O_2	0.5 M Na_2HPO_4/ NaH_2PO_4, 80 ml	-	co-catalyst free water splitting	[170] 2018

Table 1 (continued)

Cu$_7$S$_4$/*y*-MnS	0.77/2.12	1 mg	MnO_x, -	cation exchange	300 W Xe lamp	0.209 mmol g^{-1} h^{-1} H_2 0.036 mmol g^{-1} h^{-1} O_2	-, 6 ml H_2O	5.5 % at 420 nm	non-stoichiometric ratio of H_2/O_2 probably due to reactive O_2 species; possible additional contribution by surface plasmons of Cu$_7$S$_4$	[171, 172] 2017
Cu$_7$S$_4$/*y*-MnS	0.77/2.12	1 mg	-	cation exchange	300 W Xe lamp	0.718 mmol g^{-1} h^{-1} H_2	0.35 M NaS and 0.25 M Na_2SO_3, 6 ml	18.8 % at 420 nm	possible additional contribution by surface plasmons of Cu$_7$S$_4$	[171, 172] 2017
Fe_2O_3/Fe_2TiO_5/TiO_2	2.0/2.1/3.0	50 mg	-	combustion	300 W Xe lamp	0.370 mmol g^{-1} h^{-1} H_2	10 vol.% TEOA, 100 ml	-	double type II cascade heterojunction	[63] 2020
g-C_3N_4/Ag_3PO_4	2.77/2.46	5 mg	Ag, -	stirring	300 W Xe lamp (AM 1.5, near IR filter)	full spectrum: 23.56 mmol g^{-1} h^{-1} H_2 AM 1.5: approx. 13 mmol g^{-1} h^{-1} H_2 near IR: approx. 9 mmol g^{-1} h^{-1} H_2	10 % lactic acid, 50 ml	-	$NaYF_4$:Yb/Tm disks used for upconverting photoluminescence, near IR active photocatalyst	[128]
g-C_3N_4/$Bi_4Ti_3O_{12}$/$Bi_2O_2I_2$ (PS I/PS II/PS III)	2.70/2.90/2.66	40 mg	-	stirring/ hydrothermal	500 W Xe lamp (λ > 420 nm)	pure water: 24.12 mmol g^{-1} h^{-1} H_2 with TEOA: 69 mmol g^{-1} h^{-1} H_2	pure water or $6.7 \cdot 10^{-2}$ M TEOA, 100 ml	-	complicated dual direct *Z*-scheme assisted by redox mediators	[101] 2021
g-C_3N_4/(Ag)/CdS	2.46/2.32	50 mg	- (Ag)	hydrothermal	350 W Xe lamp (λ > 420 nm)	1.376 mmol g^{-1} h^{-1} H_2	10 % lactic acid, 100 ml	-	SPR effect	[123] 2018
g-C_3N_4/CdS	2.7/2.4	300 mg	Pt, 0.4 mg	stirring	350 W Xe lamp (λ > 420 nm)	10.89 mmol g^{-1} H_2	0.01 M NaS and 0.05 M Na_2SO_3, 100 ml	-	CdS@g-C_3N_4; duration of illumination unclear	[150] 2017
g-C_3N_4/CdS / P-C_3N_4/CdS	2.87/2.30	10 mg	Pt, 1	stirring (photodepos.) / hydrothermal (chemical depos.)	300 W Xe lamp (λ > 420 nm)	5.69 mmol g^{-1} h^{-1} H_2 (photodepos.) 1.49 mmol g^{-1} h^{-1} H_2 (chemical depos.)	0.05 M NaS and 0.1 M Na_2SO_3, 100 ml	10.3 % at 420 nm (photodepos.) 3.8 % at 420 nm (chemical depos.)	photodepos. leads to type II heterojunction (higher photocatalytic activity) chemical depos. leads to *Z*-scheme (lower photocatalytic activity)	[95] 2018
NCN-CN_x/(Au)/$CuInS_2$	2.7/1.6	10 mg	(Au), Pt	stirring	300 W Xe lamp (λ > 550 nm)	full spectra: 10.72 mmol g^{-1} h^{-1} H_2 with filter: 4.28 mmol g^{-1} h^{-1} H_2	10 vol.% TEOA, 100 ml	-	synergistic effects of SPR and *Z*-scheme mechanism	[125] 2021
g-C_3N_4/Cu_3P	2.72/1.50	20 mg	-	precipitation + solid state reaction	300 W Xe lamp (λ > 420 nm)	0.284 mmol g^{-1} h^{-1} H_2	10 vol.% TEOA, 80 ml	2.6 % at 420 nm	*p–n* junction; H_2 production rate 95 times higher than pure g-C_3N_4	[56] 2018
g-C_3N_4/(Ag)/NiTiO_3	2.61/2.18	4 mg	- (Ag)	stirring	300 W Xe lamp	3.351 mmol g^{-1} h^{-1} H_2	10 vol.% TEOA, 40 ml	-	synergistic effects of SPR and *Z*-scheme mechanism	[120] 2019
g-C_3N_4/(Ag)/SnS_2	2.86/2.28	100 mg	- (Ag)	hydrothermal	500 W Xe lamp (λ > 420 nm)	1.1045 mmol g^{-1} h^{-1} H_2	0.25 M Na_2S and 0.35 M Na_2SO_3, 100 ml	-	*Z*-scheme plasmonic photocatalyst with 3D flower-like SnS_2 microspheres on the 2D Ag-g-C_3N_4 nanosheets	[121] 2021
g-C_3N_4/ (Ag/Fe_2O_3)/SrTiO_3	2.7/3.14	50 mg	(Ag), Pt, 2	wet-impregnation, calcination	300 W Xe lamp	without Pt: 2.0008 mmol g^{-1} h^{-1} H_2 with Pt: 4.200 mmol g^{-1} h^{-1} H_2	10 vol.% TEOA, 55 ml	-	g-C_3N_4/SrTiO_3 junction bridged with Ag/Fe_2O_3 nanoparticles; SPR effect	[122] 2018
g-C_3N_4/(Au)/TiO_2	2.7/3.2	10 mg	- (Au)	stirring, hydrothermal	300 W Xe lamp (λ > 420 nm)	0.129 mmol g^{-1} h^{-1} H_2	10 vol.% TEOA, 20 ml	-	SPR effects of Au; enhanced light utilization of carbon doped TiO_2 hollow spheres	[173] 2017
g-C_3N_4/TiO_2	2.7/3.19	10 mg	(Ag), Pt, 1.0	stirring, calcination	350 W Xe lamp (λ > 400 nm)	6.4 mmol in 4 h (non-linear course)	10 vol.% TEOA, 10 ml	-	SPR effect	[124] 2019
g-C_3N_4/TiO_2	2.9/3.2	50 mg	Pt, 1.0	suspension, calcination	350 W Xe lamp	4.128 mmol g^{-1} h^{-1} H_2	10 vol.% TEOA, 100 ml	-	3D TiO_2 microflowers on 2D g-C_3N_4 nanosheets; *Z*-scheme charge transfer presumed only based on potential barriers	[174] 2019

Table 1 (continued)

g-C_3N_4/TiO$_2$(P25)	2.76/3.2	12.5 mg	Pd, 0.5 on TiO_2	calcination	300 W Xe lamp (λ > 400 nm)	visible light: 1.07 mmol g_{cat}^{-1} h^{-1} H_2 full wave irr.: 6.33 mmol g_{cat}^{-1} h^{-1} H_2	10 vol.% TEOA, 80 ml	-	targeted charge transfer path	[175] 2019
g-C_3N_4/TiO$_2$(P25) (QCN/x-TiO$_2$/t-TiO$_2$)	2.9/3.20/3.03	50 mg	Pt, 1	mixing, heating	300 W Xe lamp / 300 W Hg lamp (λ > 400 nm)	simulated sunlight: 0.153 mmol g_{cat}^{-1} h^{-1} H_2 visible light: 0.049 mmol g_{cat}^{-1} h^{-1} H_2	10 vol.% MeOH, 333 ml	-	further experiments regarding oxygen evolution	[176] 2020
g-C_3N_4/TiO$_2$ (black TiO$_2$)	2.6/2.44	50 mg	-	sonication, thermal annealing	300 W Xe lamp	0.809 mmol g_{cat}^{-1} h^{-1} H_2	10 vol.% TEOA, 100 ml	-	Ti^{3+} self-doped TiO_2/g-C_3N_4 hollow core-shell structure	[177] 2018
g-C_3N_4/TiO$_2$	2.7/3.2	50 mg	-	hydrothermal	300 W Xe lamp (λ > 400 nm)	0.0065 mmol g_{cat}^{-1} h^{-1} H_2	-, 100 ml	-	carbon quantum dots with upconversion fluorescence for improved visible light utilization and H_2O_2 decomposition	[134] 2018
g-C_3N_4/$W_{18}O_{49}$	2.7/3.0	5 mg	Pt, 1.0	solvothermal	320 W Xe lamp with solar filter (AM 1.5)	3.04 mmol g_{cat}^{-1} h^{-1} H_2	15 vol.% TEOA, 10 ml	-	nonmetal plasmonic Z-scheme heterostructure photocatalyst, VIS/NIR absorption due to LSPR	[126] 2017
g-C_3N_4/ZnIn$_2S_4$	2.83/2.29	50 mg	Pt, 3	solvothermal	300 W Xe lamp (λ > 420 nm)	6.095 mmol g_{cat}^{-1} h^{-1} H_2	20 vol.% TEOA, 10 ml	12.9 % at 400 nm 9.8 % at 420 nm	2D/2D vdW photocatalyst; sulphur vacancies ameliorating light absorption & trapping electrons	[58] 2020
g-C_3N_4/ZnS/ZnO (PS I/PS II/PS III)	2.7/3.67/3.37	100 mg	-	stirring	300 W Xe lamp	0.301 mmol g_{cat}^{-1} h^{-1} H_2	0.25 M NaS and 0.25 M Na_2SO_3, 100 ml	-	dual direct Z-scheme; little analysis of charge transfer mechanism	[102] 2017
In$_2$S$_3$/g-C_3N_4/TiO$_2$	2.23/3.82	60 mg	Pt, 2	self-assembling under sonication	300 W Xe lamp (λ > 400 nm)	0.159 mmol g_{cat}^{-1} h^{-1} H_2	0.05 M NaS and 0.05 M Na_2SO_3, 100 ml	-	type II *p-n* heterojunction, nanosheets in a face-to-face manner	[52] 2019
MoS$_2$/SiO$_2$	1.8/2.81	50 mg	-	hydrothermal	300 W Xe lamp (λ > 420 nm)	0.010 mmol g_{cat}^{-1} h^{-1} H_2	-	-	no O_2 production rate stated	[57] 2020
MoS$_2$/CaTiO$_3$	1.88/3.56	50 mg	Pt, 3	hydrothermal	300 W Xe lamp	0.622 mmol g_{cat}^{-1} h^{-1} H_2	0.3 M vitamin C, 100 ml	4.6 % at 350 nm	MoS_2 nanospheres on hollow $CaTiO_3$ cubes	[178] 2020
MoS$_2$/g-C_3N_4	3.41/2.91	50 mg	Pt, 2	milling	300 W Xe lamp	0.577 mmol g_{cat}^{-1} h^{-1} H_2	25 vol.% MeOH, 120 ml	-	p-type MoS_2 quantum dots on n-type g-C_3N_4 nanosheets	[179] 2018
Ni-MOF-74/CdZnS-S	2.37/2.43	10 mg	-	mixing	5 W LED	1.712 mmol over 5 h → 34.26 mmol g_{cat}^{-1} h^{-1} H_2	10 (vol.)% lactic acid, 30 ml	-	Z-scheme containing a metal organic framework (MOF)	[105] 2020
NiO/TiO$_2$	1.42/3.46	50 mg	Pt, 1	hydrothermal	300 W Xe lamp (AM 1.5 filter)	0.391 mmol g_{cat}^{-1} h^{-1} H_2	9.09 vol.% MeOH, 55 ml	-	material with Ti^{3+} and oxygen vacancies (mid gap states) showed higher photocatalytic activity	[164] 2019
NiS/TiO$_2$	1.92/3.2	50 mg	-	hydrothermal and electrospinning	350 W Xe lamp/ 250 W Hg lamp	0.655 mmol g_{cat}^{-1} h^{-1} H_2 (Xe lamp)	20 vol.% methanol, 80 ml	-	core shell hybrid: NiS nanoplates on electrospun TiO_2 nanofibers; isotope tracer test using methanol and D_2O is presented as evidence for water splitting	[180] 2018
P^{1}Ag$_3$PO$_4$	0.71/2.45	15 mg	-	stirring, high speed centrifugation	10 W laser (980 nm)	0.146 mmol g_{cat}^{-1} h^{-1} H_2	50 vol.% glycerol, 100 ml (other sacrificial agents were tested)	0.077 % at 980 nm	$NaYF_4$:Yb^{3+},Tm^{3+} used for upconverting photoluminescence, near IR active photocatalyst	[133] 2019
P/B/VO$_x$	0.7/2.39	5 mg	-	mechanical mixing	320 W Xe lamp (λ > 420 nm)	0.16 mmol g_{cat}^{-1} h^{-1} H_2 0.102 mmol g_{cat}^{-1} h^{-1} O_2	-, 8 ml H_2O	0.89 % at 420 nm	water splitting on a 2D heterostructure	[137, 138] 2018
P/P (BP/RP)	1.27/1.96	2 mg	Co, Fe, Ni, Cu	solvothermal	LED light (20×10 W, λ > 420 nm)	0.33 mmol g_{cat}^{-1} h^{-1} H_2 without co-cat.; approx. 3 mmol g_{cat}^{-1} h^{-1} H_2 with Co co-cat.	-, 6 ml H_2O	1.21 % at 420 nm	oxidation species: H_2O_2 (attributed to the combination of two hydroxyl radicals)	[154, 155] 2019
Ta$_3$N$_5$/ZnO	2.0/3.2	unclear (fixed on Si subs.)	-	ALD	300 W Xe lamp	0.500 mmol g_{cat}^{-1} h^{-1} H_2	20 vol.% MeOH, 25 ml	-		[181] 2018
TiO$_2$/Ta$_2$O$_5$	3.12/3.85	100 mg	An, -	ultrasound, calcination	300 W Xe lamp (visible light filter), cut-off wavelength not given	0.159 mmol g_{cat}^{-1} H_2 over 5 h → 0.032 mmol g_{cat}^{-1} h^{-1} H_2	MeOH, -	-	Er^{3+}:$YAlO_3$ as up-conversion luminescence agent (from visible- light to ultraviolet-light); Z-scheme established by a TiO$_2$-Fe^{2+}/V^{5+}-Ta$_2$O$_5$ redox cycle system	[135] 2018
TiO$_2$/WO$_3$	3.2/2.8	50 mg	Au, up to 0.45 wt.%	electrospinning	300 W Xe lamp	0.2696 mmol h^{-1} H_2 → 5.938 mmol g_{cat}^{-1} h^{-1} H_2	36 vol.% MeOH, 70 ml	-	enhanced activity attributed to synergistic effect of Schottky junc. and SPR	[115] 2017
TiO$_2$/(Pt)/WO$_3$	3.2/2.8	50 mg	(Pt), Au	electrospinning	300 W Xe lamp	0.242 mmol g_{cat}^{-1} h^{-1} H_2	38 vol.% MeOH, 65 ml	-	plasmon-enhanced charged separation	[117] 2017
TpPa-S_2/COF/ a-WO$_3$	2.04/2.07	10 mg	-	solvothermal	300 W Xe lamp (λ > 420 nm)	3.77 mmol g_{cat}^{-1} h^{-1} H_2	0.1 M phosphate-buffered saline (PBS) at pH = 7 containing 100 mg sodium ascorbate, 50 ml	0.137 % at 450 nm	first reported covalent-organic framework (COF) based Z-scheme	[111] 2020
Zn$_x$Cd$_{1-x}$S/ZnO	2.50 to 2.79	25 mg	-	topotactic sulfurization/ oxidization	300 W Xe lamp (λ > 420 nm)	38.93 mmol g_{cat}^{-1} h^{-1} H_2	0.1 Na_2S and 0.1 M Na_2SO_3, 100 ml	40.97 % at 420 nm	educt: ZnCdAl layer double hydroxide (LDH)	[144] 2018
Zn$_{1-x}$Cd$_x$S/ZnO$_{1-y}$	2.52/3.2	100 mg	Pd, 0.1	calcination	300 W Xe lamp (λ > 420 nm)	without Pd: 25.18 mmol g_{cat}^{-1} h^{-1} H_2 with Pd: 37.79 mmol g_{cat}^{-1} h^{-1} H_2	0.1 Na_2S and 0.1 M Na_2SO_3, 100 ml	without Pd: 49.5 % at 420 nm with Pd: 62.1 % at 420 nm	extremely high AQE; oxygen vacancies enhance light absorption	[182] 2017
ZnIn$_2$S$_4$/(Ti)O-(6-(COOH)$_2$	2.64/3.62	40 mg	MoS_2, 2	solvothermal	300 W Xe lamp	18.794 mmol g_{cat}^{-1} h^{-1} H_2	0.70 M Na_2S and 0.5 M Na_2SO_3, 100 ml	-	Z-scheme containing a metal organic framework (MOF), Z-scheme charge transfer only based on produced species and Fermi levels	[106] 2020
ZnIn$_2$S$_4$/WO$_3$	2.37/2.58	5 mg	NiS, quantum dots	mixing/ refluxing	300 W Xe lamp	without NiS: 7.81 mmol g_{cat}^{-1} h^{-1} H_2 with NiS: 11.09 mmol g_{cat}^{-1} h^{-1} H_2	10 vol.% lactic acid, -	72 % at 420 nm	Janus sulphur vacancy rich Z-scheme; highest activity among the family of ZnIn$_2$S$_4$ materials	[139] 2019
ZnS/CdS/TaON	-/2.4/2.71	100 mg	-	sol-gel	300 W Xe lamp with solar filter (AM 1.5)/ cut-off filter (λ > 420 nm)	0.8396 mmol g_{cat}^{-1} h^{-1} H_2	0.35 M Na_2S and 0.25 M Na_2SO_3, 100 ml	-	14 times higher H_2 evolution activity compared to CdS/TaON	[67] 2019
ZnTe/TiO$_2$	2.14/3.05	50 mg	Au, 2	hydrothermal	320 W Xe lamp (350 nm < λ < 800 nm)	3.34 mmol g_{cat}^{-1} h^{-1} H_2 H_2 and O_2 with a ratio of 2 : 1	-, 50 ml H_2O	-	SPR enhanced Z-Scheme; core-shell TiO_2/ZnTe coaxial nanorods; no O_2 production rate stated	[183] 2019

Funding Open Access funding enabled and organized by Projekt DEAL.

Declarations

Conflict of interest On behalf of all authors, the corresponding author states that there is no conflict of interest.

References

1. Brown D (2016) US and world hydrogen production—2014. CryoGas Int, Lexington
2. Ausfelder F, Bazzanella A (2016) Hydrogen in the chemical industry. Hydrog Sci Eng Mater Process Syst Technol 10:19–40
3. Dawood F, Anda M, Shafiullah GM (2020) Hydrogen production for energy: an overview. Int J Hydrogen Energy 45:3847–3869
4. Oliveira AM, Beswick RR, Yan Y (2021) A green hydrogen economy for a renewable energy society. Curr Opin Chem Eng 33:100701. https://doi.org/10.1016/j.coche.2021.100701
5. Haszeldine RS (2009) Carbon capture and storage: how green can black be? Science (80–) 325:1647–1652. https://doi.org/10.1126/science.1172246
6. Marschall R (2021) 50 years of materials research for photocatalytic water splitting. Eur J Inorg Chem 2021:2435–2441. https://doi.org/10.1002/ejic.202100264
7. Edwards PP, Kuznetsov VL, David WIF, Brandon NP (2008) Hydrogen and fuel cells: towards a sustainable energy future. Energy Policy 36:4356–4362. https://doi.org/10.1016/j.enpol.2008.09.036
8. Thomas JM, Edwards PP, Dobson PJ, Owen GP (2020) Decarbonising energy: the developing international activity in hydrogen technologies and fuel cells. J Energy Chem 51:405–415. https://doi.org/10.1016/j.jechem.2020.03.087
9. Yilmaz C, Wendelstorf J, Turek T (2017) Modeling and simulation of hydrogen injection into a blast furnace to reduce carbon dioxide emissions. J Clean Prod 154:488–501. https://doi.org/10.1016/j.jclepro.2017.03.162
10. Bicer Y, Dincer I, Vezina G, Raso F (2017) Impact assessment and environmental evaluation of various ammonia production processes. Environ Manage 59:842–855
11. Ursua A, Gandia LM, Sanchis P (2011) Hydrogen production from water electrolysis: current status and future trends. Proc IEEE 100:410–426
12. Moussallem I, Pinnow S, Wagner N, Turek T (2012) Development of high-performance silver-based gas-diffusion electrodes for chlor-alkali electrolysis with oxygen depolarized cathodes. Chem Eng Process Process Intensif 52:125–131. https://doi.org/10.1016/j.cep.2011.11.003
13. Kayfeci M, Keçebaş A, Bayat M (2019) Chapter 3—hydrogen production. In: Calise F, D'Accadia MD, Santarelli M et al (eds) Solar hydrogen production. Academic Press, London, pp 45–83
14. Penner SS (2006) Steps toward the hydrogen economy. Energy 31:33–43. https://doi.org/10.1016/j.energy.2004.04.060
15. Clark WW, Rifkin J (2006) A green hydrogen economy. Energy Policy 34:2630–2639. https://doi.org/10.1016/j.enpol.2005.06.024

16. Brandon NP, Kurban Z (2017) Clean energy and the hydrogen economy. Philos Trans R Soc A Math Phys Eng Sci 375:20160400
17. Ball M, Weeda M (2015) The hydrogen economy–vision or reality? Int J Hydrog Energy 40:7903–7919
18. Bockris JO (1972) A hydrogen economy. Science (80–) 176:1323
19. Koumi Ngoh S, Njomo D (2012) An overview of hydrogen gas production from solar energy. Renew Sustain Energy Rev 16:6782–6792. https://doi.org/10.1016/j.rser.2012.07.027
20. Marschall R (2014) Semiconductor composites: strategies for enhancing charge carrier separation to improve photocatalytic activity. Adv Funct Mater 24:2421–2440. https://doi.org/10.1002/adfm.201303214
21. Takanabe K (2017) Photocatalytic water splitting: quantitative approaches toward photocatalyst by design. ACS Catal 7:8006–8022. https://doi.org/10.1021/acscatal.7b02662
22. Li Y, Tsang SCE (2020) Recent progress and strategies for enhancing photocatalytic water splitting. Mater Today Sustain 9:100032
23. Li X, Yu J, Low J et al (2015) Engineering heterogeneous semiconductors for solar water splitting. J Mater Chem A 3:2485–2534
24. Maeda K, Domen K (2010) Photocatalytic water splitting: recent progress and future challenges. J Phys Chem Lett 1:2655–2661. https://doi.org/10.1021/jz1007966
25. Kanan MW, Nocera DG (2008) In situ formation of an oxygen-evolving catalyst in neutral water containing phosphate and Co2+. Science (80–) 321:1072–1075
26. Osterloh FE (2017) Photocatalysis versus photosynthesis: a sensitivity analysis of devices for solar energy conversion and chemical transformations. ACS Energy Lett 2:445–453. https://doi.org/10.1021/acsenergylett.6b00665
27. Kudo A, Miseki Y (2009) Heterogeneous photocatalyst materials for water splitting. Chem Soc Rev 38:253–278. https://doi.org/10.1039/b800489g
28. Chen X, Shen S, Guo L, Mao SS (2010) Semiconductor-based photocatalytic hydrogen generation. Chem Rev 110:6503–6570. https://doi.org/10.1021/cr1001645
29. Moss B, Wang Q, Butler KT et al (2021) Linking in situ charge accumulation to electronic structure in doped $SrTiO_3$ reveals design principles for hydrogen-evolving photocatalysts. Nat Mater 20:511–517. https://doi.org/10.1038/s41563-020-00868-2
30. Modak B, Ghosh SK (2015) Exploring the role of La codoping beyond charge compensation for enhanced hydrogen evolution by Rh–$SrTiO_3$. J Phys Chem B 119:11089–11098. https://doi.org/10.1021/acs.jpcb.5b02906
31. Zhao ZV, Goncalves R, Barman KS et al (2019) Electronic structure basis for enhanced overall water splitting photocatalysis with aluminum doped $SrTiO_3$ in natural sunlight. Energy Environ Sci 12:1385–1395. https://doi.org/10.1039/C9EE00310J
32. Yang J, Wang D, Han H, Li CAN (2013) Roles of cocatalysts in photocatalysis and photoelectrocatalysis. Acc Chem Res 46:1900–1909
33. Maeda K, Lu D, Teramura K, Domen K (2008) Direct deposition of nanoparticulate rhodium–chromium mixed-oxides on a semiconductor powder by band-gap irradiation. J Mater Chem 18:3539–3542. https://doi.org/10.1039/B808484J
34. Maeda K, Ohno T, Domen K (2011) A copper and chromium based nanoparticulate oxide as a noble-metal-free cocatalyst for photocatalytic water splitting. Chem Sci 2:1362–1368. https://doi.org/10.1039/C1SC00177A
35. Zong X, Yan H, Wu G et al (2008) Enhancement of photocatalytic H_2 evolution on CdS by loading MoS_2 as cocatalyst under visible light irradiation. J Am Chem Soc 130:7176–7177. https://doi.org/10.1021/ja8007825
36. Yan H, Yang J, Ma G et al (2009) Visible-light-driven hydrogen production with extremely high quantum efficiency on Pt–PdS/CdS photocatalyst. J Catal 266:165–168. https://doi.org/10.1016/j.jcat.2009.06.024
37. Schneider J, Bahnemann DW (2013) Undesired role of sacrificial reagents in photocatalysis. J Phys Chem Lett 4:3479–3483. https://doi.org/10.1021/jz4018199
38. Kawai T, Sakata T (1980) Photocatalytic hydrogen production from liquid methanol and water. J Chem Soc Chem Commun 20:694–695
39. Kandiel TA, Dillert R, Robben L, Bahnemann DW (2011) Photonic efficiency and mechanism of photocatalytic molecular hydrogen production over platinized titanium dioxide from aqueous methanol solutions. Catal Today 161:196–201. https://doi.org/10.1016/j.cattod.2010.08.012

40. Afroz K, Moniruddin M, Bakranov N et al (2018) A heterojunction strategy to improve the visible light sensitive water splitting performance of photocatalytic materials. J Mater Chem A 6:21696–21718. https://doi.org/10.1039/C8TA04165B
41. Sun K, Jing Y, Li C et al (2012) 3D branched nanowire heterojunction photoelectrodes for high-efficiency solar water splitting and H 2 generation. Nanoscale 4:1515–1521. https://doi.org/10.1039/C2NR11952H
42. Hou Y, Zuo F, Dagg A, Feng P (2012) Visible light-driven α-Fe_2O_3 nanorod/graphene/BiV_1–$xMoxO_4$ core/shell heterojunction array for efficient photoelectrochemical water splitting. Nano Lett 12:6464–6473. https://doi.org/10.1021/nl303961c
43. Xiang Q, Yu J, Jaroniec M (2011) Preparation and enhanced visible-light photocatalytic H_2-production activity of graphene/C_3N_4 composites. J Phys Chem C 115:7355–7363. https://doi.org/10.1021/jp200953k
44. Nasir SNFM, Ullah H, Ebadi M et al (2017) New insights into Se/$BiVO_4$ heterostructure for photoelectrochemical water splitting: a combined experimental and DFT study. J Phys Chem C 121:6218–6228. https://doi.org/10.1021/acs.jpcc.7b01149
45. Lou Z, Li F, Deng J et al (2013) Branch-like hierarchical heterostructure (α-Fe_2O_3/TiO_2): a novel sensing material for trimethylamine gas sensor. ACS Appl Mater Interfaces 5:12310–12316. https://doi.org/10.1021/am402532v
46. Watanabe MO, Yoshida J, Mashita M et al (1985) Band discontinuity for GaAs/AlGaAs heterojunction determined by C-V profiling technique. J Appl Phys 57:5340–5344
47. Moniz ASJ, Shevlin AS, James Martin D et al (2015) Visible-light driven heterojunction photocatalysts for water splitting—a critical review. Energy Environ Sci 8:731–759. https://doi.org/10.1039/C4EE03271C
48. Shim J, Oh S, Kang D-H et al (2016) Phosphorene/rhenium disulfide heterojunction-based negative differential resistance device for multi-valued logic. Nat Commun 7:13413. https://doi.org/10.1038/ncomms13413
49. Wang H, Zhang L, Chen Z et al (2014) Semiconductor heterojunction photocatalysts: design, construction, and photocatalytic performances. Chem Soc Rev 43:5234–5244
50. Low J, Yu J, Jaroniec M et al (2017) Heterojunction photocatalysts. Adv Mater 29:1601694
51. Wang Z, Lin Z, Shen S et al (2021) Advances in designing heterojunction photocatalytic materials. Chin J Catal 42:710–730. https://doi.org/10.1016/S1872-2067(20)63698-1
52. Hua E, Jin S, Wang X et al (2019) Ultrathin 2D type-II pn heterojunctions $La_2Ti_2O_7$/In_2S_3 with efficient charge separations and photocatalytic hydrogen evolution under visible light illumination. Appl Catal B Environ 245:733–742
53. Kumar R, Das D, Singh AK (2018) C_2N/WS_2 van der Waals type-II heterostructure as a promising water splitting photocatalyst. J Catal 359:143–150
54. Wang B, Yuan H, Chang J et al (2019) Two dimensional InSe/C_2N van der Waals heterojunction as enhanced visible-light-responsible photocatalyst for water splitting. Appl Surf Sci 485:375–380
55. Zhang X, Chen A, Zhang Z et al (2019) Rational design of C_2N-based type-II heterojunctions for overall photocatalytic water splitting. Nanosc Adv 1:154–161
56. Qin Z, Wang M, Li R, Chen Y (2018) Novel Cu_3P/g-C_3N_4 pn heterojunction photocatalysts for solar hydrogen generation. Sci China Mater 61:861–868
57. Khalid NR, Israr Z, Tahir MB, Iqbal T (2020) Highly efficient Bi_2O_3/MoS_2 pn heterojunction photocatalyst for H_2 evolution from water splitting. Int J Hydrog Energy 45:8479–8489
58. Qin Y, Li H, Lu J et al (2020) Synergy between van der Waals heterojunction and vacancy in $ZnIn_2S_4$/g-C_3N_4 2D/2D photocatalysts for enhanced photocatalytic hydrogen evolution. Appl Catal B Environ 277:119254
59. Zeng J, Xu L, Luo X et al (2021) A novel design of SiH/CeO_2 (111) van der Waals type-II heterojunction for water splitting. Phys Chem Chem Phys 23:2812–2818. https://doi.org/10.1039/D0CP05238H
60. Zhao Z, Willard EJ, Dominguez JR et al (2019) Depletion layer controls photocatalytic hydrogen evolution with p-type gallium phosphide particles. J Mater Chem A 7:18020–18029. https://doi.org/10.1039/C9TA05879F
61. Papp J, Soled S, Dwight K, Wold A (1994) Surface acidity and photocatalytic activity of TiO_2, WO_3/TiO_2, and MoO_3/TiO_2 photocatalysts. Chem Mater 6:496–500. https://doi.org/10.1021/cm00040a026

62. Zhou B-X, Ding S-S, Wang Y et al (2020) Type-II/type-II band alignment to boost spatial charge separation: a case study of g-C_3N_4 quantum dots/a-TiO_2/r-TiO_2 for highly efficient photocatalytic hydrogen and oxygen evolution. Nanoscale 12:6037–6046. https://doi.org/10.1039/D0NR00176G
63. Bhoi YP, Fang F, Zhou X et al (2020) Single step combustion synthesis of novel Fe_2TiO_5/α-Fe_2O_3/TiO_2 ternary photocatalyst with combined double type-II cascade charge migration processes and efficient photocatalytic activity. Appl Surf Sci 525:146571. https://doi.org/10.1016/j.apsusc.2020.146571
64. Galedari M, Mehdipour Ghazi M, Mirmasoomi SR (2021) Novel visible-driven Ag_2O/Fe_2O_3/TiO_2 nano sized hetero-structured photocatalyst: synthesis, characterization and photo-degradation of tetracycline. Chem Eng Res Des 170:248–255. https://doi.org/10.1016/j.cherd.2021.04.008
65. Ke T, Shen S, Yang K, Lin D (2022) In situ fabrication of Bi_2O_3/C_3N_4/TiO_2@C photocatalysts for visible-light photodegradation of sulfamethoxazole in water. Appl Surf Sci 580:152302. https://doi.org/10.1016/j.apsusc.2021.152302
66. Zhong Y, Wu Y, Chang B et al (2019) A CoP/CdS/WS_2 p–n–n tandem heterostructure: a novel photocatalyst for hydrogen evolution without using sacrificial agents. J Mater Chem A 7:14638–14645. https://doi.org/10.1039/C9TA03721G
67. An L, Han X, Li Y et al (2019) ZnS–CdS–TaON nanocomposites with enhanced stability and photocatalytic hydrogen evolution activity. J Sol-Gel Sci Technol 91:82–91. https://doi.org/10.1007/s10971-019-05009-z
68. Das K, Bariki R, Majhi D et al (2022) Facile synthesis and application of CdS/$Bi_{20}TiO_{32}$/$Bi_4Ti_3O_{12}$ ternary heterostructure: a synergistic multi-heterojunction photocatalyst for enhanced endosulfan degradation and hydrogen evolution reaction. Appl Catal B Environ 303:120902. https://doi.org/10.1016/j.apcatb.2021.120902
69. Maeda K (2013) Z-scheme water splitting using two different semiconductor photocatalysts. ACS Catal 3:1486–1503. https://doi.org/10.1021/cs4002089
70. Bard AJ (1979) Photoelectrochemistry and heterogeneous photo-catalysis at semiconductors. J Photochem 10:59–75. https://doi.org/10.1016/0047-2670(79)80037-4
71. Abe R, Sayama K, Sugihara H (2005) Development of new photocatalytic water splitting into H_2 and O_2 using two different semiconductor photocatalysts and a shuttle redox mediator IO_3-/I. J Phys Chem B 109:16052–16061
72. Abe R, Higashi M, Domen K (2011) Overall water splitting under visible light through a two-step photoexcitation between TaON and WO_3 in the presence of an iodate-iodide shuttle redox mediator. Chemsuschem 4:228–237
73. Maeda K, Higashi M, Lu D et al (2010) Efficient nonsacrificial water splitting through two-step photoexcitation by visible light using a modified oxynitride as a hydrogen evolution photocatalyst. J Am Chem Soc 132:5858–5868. https://doi.org/10.1021/ja1009025
74. Abe R, Sayama K, Arakawa H (2003) Significant influence of solvent on hydrogen production from aqueous I_3-/I-redox solution using dye-sensitized Pt/TiO_2 photocatalyst under visible light irradiation. Chem Phys Lett 379:230–235
75. Kato H, Sasaki Y, Iwase A, Kudo A (2007) Role of iron ion electron mediator on photocatalytic overall water splitting under visible light irradiation using Z-scheme systems. Bull Chem Soc Jpn 80:2457–2464
76. Sasaki Y, Iwase A, Kato H, Kudo A (2008) The effect of co-catalyst for Z-scheme photocatalysis systems with an Fe^{3+}/Fe^{2+} electron mediator on overall water splitting under visible light irradiation. J Catal 259:133–137
77. Xu Q, Zhang L, Yu J et al (2018) Direct Z-scheme photocatalysts: principles, synthesis, and applications. Mater Today 21:1042–1063. https://doi.org/10.1016/j.mattod.2018.04.008
78. Liu X, Zhang Q, Ma D (2021) Advances in 2D/2D Z-scheme heterojunctions for photocatalytic applications. Sol RRL 5:2000397. https://doi.org/10.1002/solr.202000397
79. Li H, Tu W, Zhou Y, Zou Z (2016) Z-Scheme photocatalytic systems for promoting photocatalytic performance: recent progress and future challenges. Adv Sci 3:1500389
80. Tada H, Mitsui T, Kiyonaga T et al (2006) All-solid-state Z-scheme in CdS–Au–TiO_2 three-component nanojunction system. Nat Mater 5:782–786
81. Zhou P, Yu J, Jaroniec M (2014) All-solid-state Z-scheme photocatalytic systems. Adv Mater 26:4920–4935

82. Li X, Garlisi C, Guan Q et al (2021) A review of material aspects in developing direct Z-scheme photocatalysts. Mater Today 47:75–107. https://doi.org/10.1016/j.mattod.2021.02.017
83. Yu J, Wang S, Low J, Xiao W (2013) Enhanced photocatalytic performance of direct Z-scheme g-C_3N_4–TiO_2 photocatalysts for the decomposition of formaldehyde in air. Phys Chem Chem Phys 15:16883–16890. https://doi.org/10.1039/C3CP53131G
84. Li H, Ba G, Liang Z et al (2019) Construction of direct all-solid-state Z-scheme p-n copper indium disulfide/tungsten oxide heterojunction photocatalysts: function of interfacial electric field. J Colloid Interface Sci 555:72–81. https://doi.org/10.1016/j.jcis.2019.07.073
85. Zhang J, Xin J, Shao C et al (2019) Direct Z-scheme heterostructure of p-$CuAl_2O_4$/n-Bi_2WO_6 composite nanofibers for efficient overall water splitting and photodegradation. J Colloid Interface Sci 550:170–179. https://doi.org/10.1016/j.jcis.2019.04.099
86. Aguirre ME, Zhou R, Eugene AJ et al (2017) Cu_2O/TiO_2 heterostructures for CO_2 reduction through a direct Z-scheme: protecting Cu_2O from photocorrosion. Appl Catal B Environ 217:485–493. https://doi.org/10.1016/j.apcatb.2017.05.058
87. Zhou FQ, Fan JC, Xu QJ, Min YL (2017) $BiVO_4$ nanowires decorated with CdS nanoparticles as Z-scheme photocatalyst with enhanced H_2 generation. Appl Catal B Environ 201:77–83
88. Xu Q, Zhang L, Cheng B et al (2020) S-scheme heterojunction. Photocatalyst Chem 6:1543–1559. https://doi.org/10.1016/j.chempr.2020.06.010
89. Zhang L, Zhang J, Yu H, Yu J (2022) Emerging S-scheme photocatalyst. Adv Mater 1:2107668. https://doi.org/10.1002/adma.202107668
90. Fu J, Xu Q, Low J et al (2019) Ultrathin 2D/2D WO3/g-C_3N_4 step-scheme H_2-production photocatalyst. Appl Catal B Environ 243:556–565
91. Liu G, Jimmy CY, Lu GQM, Cheng H-M (2011) Crystal facet engineering of semiconductor photocatalysts: motivations, advances and unique properties. Chem Commun 47:6763–6783
92. Bai S, Wang L, Li Z, Xiong Y (2017) Facet-engineered surface and interface design of photocatalytic materials. Adv Sci 4:1600216
93. Yu J, Low J, Xiao W et al (2014) Enhanced photocatalytic CO_2-reduction activity of anatase TiO_2 by coexposed 001 and 101 facets. J Am Chem Soc 136:8839–8842
94. Huang Z, Sun Q, Lv K et al (2015) Effect of contact interface between TiO_2 and g-C_3N_4 on the photoreactivity of g-C_3N_4/TiO_2 photocatalyst: (001) vs (101) facets of TiO_2. Appl Catal B Environ 164:420–427. https://doi.org/10.1016/j.apcatb.2014.09.043
95. Jiang W, Zong X, An L et al (2018) Consciously constructing heterojunction or direct Z-scheme photocatalysts by regulating electron flow direction. ACS Catal 8:2209–2217. https://doi.org/10.1021/acscatal.7b04323
96. Jiang W, Qu D, An L et al (2019) Deliberate construction of direct Z-scheme photocatalysts through photodeposition. J Mater Chem A 7:18348–18356. https://doi.org/10.1039/C9TA05607F
97. Wang M, Tan G, Ren H et al (2019) Direct double Z-scheme Og-C_3N_4/Zn_2SnO_4N/ZnO ternary heterojunction photocatalyst with enhanced visible photocatalytic activity. Appl Surf Sci 492:690–702
98. Zhu M, Liu Q, Chen W et al (2017) Boosting the visible-light photoactivity of BiOCl/$BiVO_4$/N-GQD ternary heterojunctions based on internal Z-scheme charge transfer of N-GQDs: simultaneous band gap narrowing and carrier lifetime prolonging. ACS Appl Mater Interfaces 9:38832–38841
99. Xue W, Huang D, Li J et al (2019) Assembly of AgI nanoparticles and ultrathin g-C_3N_4 nanosheets codecorated Bi_2WO_6 direct dual Z-scheme photocatalyst: an efficient, sustainable and heterogeneous catalyst with enhanced photocatalytic performance. Chem Eng J 373:1144–1157
100. Zheng J, Zhang L (2019) Designing 3D magnetic peony flower-like cobalt oxides/g-C_3N_4 dual Z-scheme photocatalyst for remarkably enhanced sunlight driven photocatalytic redox activity. Chem Eng J 369:947–956
101. Kumar A, Sharma G, Kumari A et al (2021) Construction of dual Z-scheme g-C_3N_4/$Bi_4Ti_3O_{12}$/$Bi_4O_5I_2$ heterojunction for visible and solar powered coupled photocatalytic antibiotic degradation and hydrogen production: boosting via I-/I_3- and Bi^{3+}/Bi^{5+} redox mediators. Appl Catal B Environ 284:119808
102. Dong Z, Wu Y, Thirugnanam N, Li G (2018) Double Z-scheme ZnO/ZnS/g-C_3N_4 ternary structure for efficient photocatalytic H_2 production. Appl Surf Sci 430:293–300
103. Liu J, Chen L, Cui H et al (2014) Applications of metal–organic frameworks in heterogeneous supramolecular catalysis. Chem Soc Rev 43:6011–6061

104. Chen Q, Li J, Cheng L, Liu H (2020) Construction of $CdLa_2S_4$/MIL-88A(Fe) heterojunctions for enhanced photocatalytic H_2-evolution activity via a direct Z-scheme electron transfer. Chem Eng J 379:122389. https://doi.org/10.1016/j.cej.2019.122389
105. Li M, Li J, Jin Z (2020) 0D/2D spatial structure of $CdxZn_1-xS$/Ni-MOF-74 for efficient photocatalytic hydrogen evolution. Dalt Trans 49:5143–5156. https://doi.org/10.1039/D0DT00271B
106. Mu F, Cai Q, Hu H et al (2020) Construction of 3D hierarchical microarchitectures of Z-scheme UiO-66-(COOH)2/$ZnIn_2S_4$ hybrid decorated with non-noble MoS_2 cocatalyst: a highly efficient photocatalyst for hydrogen evolution and Cr(VI) reduction. Chem Eng J 384:123352. https://doi.org/10.1016/j.cej.2019.123352
107. Liu B, Vikrant K, Kim K-H et al (2020) Critical role of water stability in metal–organic frameworks and advanced modification strategies for the extension of their applicability. Environ Sci Nano 7:1319–1347
108. You J, Zhao Y, Wang L, Bao W (2021) Recent developments in the photocatalytic applications of covalent organic frameworks: a review. J Clean Prod 291:125822
109. Pachfule P, Acharjya A, Roeser J et al (2018) Diacetylene functionalized covalent organic framework (COF) for photocatalytic hydrogen generation. J Am Chem Soc 140:1423–1427
110. Wang X, Chen L, Chong SY et al (2018) Sulfone-containing covalent organic frameworks for photocatalytic hydrogen evolution from water. Nat Chem 10:1180–1189
111. Zhang Y-P, Tang H-L, Dong H et al (2020) Covalent-organic framework based Z-scheme heterostructured noble-metal-free photocatalysts for visible-light-driven hydrogen evolution. J Mater Chem A 8:4334–4340. https://doi.org/10.1039/C9TA12870K
112. Li H, Zhang L (2017) Photocatalytic performance of different exposed crystal facets of BiOCl. Curr Opin Green Sustain Chem 6:48–56. https://doi.org/10.1016/j.cogsc.2017.05.005
113. Wang M, Ye M, Iocozzia J et al (2016) Plasmon-mediated solar energy conversion via photocatalysis in noble metal/semiconductor composites. Adv Sci 3:1600024. https://doi.org/10.1002/advs.201600024
114. Yuan L, Weng B, Colmenares JC et al (2017) Multichannel charge transfer and mechanistic insight in metal decorated 2D–2D Bi_2WO_6–TiO_2 cascade with enhanced photocatalytic performance. Small 13:1702253. https://doi.org/10.1002/smll.201702253
115. Gao H, Zhang P, Zhao J et al (2017) Plasmon enhancement on photocatalytic hydrogen production over the Z-scheme photosynthetic heterojunction system. Appl Catal B Environ 210:297–305. https://doi.org/10.1016/j.apcatb.2017.03.050
116. Fu J, Cao S, Yu J (2015) Dual Z-scheme charge transfer in TiO_2–Ag–Cu_2O composite for enhanced photocatalytic hydrogen generation. J Mater 1:124–133. https://doi.org/10.1016/j.jmat.2015.02.002
117. Zhao J, Zhang P, Wang Z et al (2017) Direct evidence of multichannel-improved charge-carrier mechanism for enhanced photocatalytic H2 evolution. Sci Rep 7:16116. https://doi.org/10.1038/s41598-017-12203-y
118. Zhao H, Li C-F, Hu Z-Y et al (2021) Size effect of bifunctional gold in hierarchical titanium oxide-gold-cadmium sulfide with slow photon effect for unprecedented visible-light hydrogen production. J Colloid Interface Sci 604:131–140. https://doi.org/10.1016/j.jcis.2021.06.167
119. Zou Y, Shi J-W, Ma D et al (2017) Fabrication of g-C_3N_4/Au/C-TiO_2 hollow structures as visible-light-driven Z-scheme photocatalysts with enhanced photocatalytic H_2 evolution. ChemCatChem 9:3752–3761. https://doi.org/10.1002/cctc.201700542
120. Kim S-R, Jo W-K (2019) Application of a photostable silver-assisted Z-scheme $NiTiO_3$ nanorod/g-C_3N_4 nanocomposite for efficient hydrogen generation. Int J Hydrogen Energy 44:801–808. https://doi.org/10.1016/j.ijhydene.2018.11.014
121. Zhao W, Li Y, Zhao P et al (2021) Novel Z-scheme Ag-C_3N_4/SnS_2 plasmonic heterojunction photocatalyst for degradation of tetracycline and H_2 production. Chem Eng J 405:126555. https://doi.org/10.1016/j.cej.2020.126555
122. Kumar A, Rana A, Sharma G et al (2018) High-performance photocatalytic hydrogen production and degradation of levofloxacin by wide spectrum-responsive Ag/Fe_3O_4 bridged $SrTiO_3$/g-C_3N_4 plasmonic nanojunctions: joint effect of Ag and Fe_3O_4. ACS Appl Mater Interfaces 10:40474–40490. https://doi.org/10.1021/acsami.8b12753
123. Qian L, Hou Y, Yu Z et al (2018) Metal-induced Z-scheme CdS/Ag/g-C_3N_4 photocatalyst for enhanced hydrogen evolution under visible light: the synergy of MIP effect and electron mediator of Ag. Mol Catal 458:43–51. https://doi.org/10.1016/j.mcat.2018.07.027

124. Geng R, Yin J, Zhou J et al (2019) In situ construction of Ag/TiO_2/g-C_3N_4 heterojunction nanocomposite based on hierarchical co-assembly with sustainable hydrogen evolution. Nanomaterials 10:1. https://doi.org/10.3390/nano10010001
125. Zhang R, Wang H, Li Y et al (2021) Investigation on the photocatalytic hydrogen evolution properties of Z-scheme Au NPs/CuInS 2 /NCN-CN x composite photocatalysts. ACS Sustain Chem Eng 9:7286–7297. https://doi.org/10.1021/acssuschemeng.1c01234
126. Zhang Z, Huang J, Fang Y et al (2017) A Nonmetal plasmonic Z-scheme photocatalyst with UV- to NIR-driven photocatalytic protons reduction. Adv Mater 29:1606688. https://doi.org/10.1002/adma.201606688
127. Li J, Lou Z, Li B (2021) Nanostructured materials with localized surface plasmon resonance for photocatalysis. Chin Chem Lett. https://doi.org/10.1016/j.cclet.2021.07.059
128. Murali G, Vattikuti SVP, Kshetri YK et al (2021) Near-infrared-activated Z-scheme NaYF4: Yb/Tm@ Ag_3PO_4/Ag@ g-C_3N_4 photocatalyst for enhanced H_2 evolution under simulated solar light irradiation. Chem Eng J 421:129687
129. Kumar A, Kumar A, Chand H, Krishnan V (2022) Upconversion nanomaterials for photocatalytic applications. Upconversion nanophosphors. Elsevier, New York, pp 391–406
130. Duan C, Liang L, Li L et al (2018) Recent progress in upconversion luminescence nanomaterials for biomedical applications. J Mater Chem B 6:192–209
131. Sun Q-C, Mundoor H, Ribot JC et al (2014) Plasmon-enhanced energy transfer for improved upconversion of infrared radiation in doped-lanthanide nanocrystals. Nano Lett 14:101–106
132. Chen G, Qiu H, Prasad PN, Chen X (2014) Upconversion nanoparticles: design, nanochemistry, and applications in theranostics. Chem Rev 114:5161–5214. https://doi.org/10.1021/cr400425h
133. Zhang Y, Wang L, Park SH et al (2019) Single near-infrared-laser driven Z-scheme photocatalytic H_2 evolution on upconversion material@Ag_3PO_4@black phosphorus. Chem Eng J 375:121967. https://doi.org/10.1016/j.cej.2019.121967
134. Pan J, You M, Chi C et al (2018) The two dimension carbon quantum dots modified porous g-C 3 N 4 /TiO 2 nano-heterojunctions for visible light hydrogen production enhancement. Int J Hydrogen Energy 43:6586–6593. https://doi.org/10.1016/j.ijhydene.2018.02.067
135. Wang G, Ma X, Wei S et al (2018) Highly efficient visible-light driven photocatalytic hydrogen production from a novel Z-scheme Er_{3+}:$YAlO_3$/Ta_2O_5-V^{5+}‖Fe_{3+}-TiO^2/Au coated composite. J Power Sources 373:161–171. https://doi.org/10.1016/j.jpowsour.2017.11.005
136. Tan C, Cao X, Wu X-J et al (2017) Recent advances in ultrathin two-dimensional nanomaterials. Chem Rev 117:6225–6331
137. Zhu M, Sun Z, Fujitsuka M, Majima T (2018) Z-scheme photocatalytic water splitting on a 2D heterostructure of black phosphorus/bismuth vanadate using visible light. Angew Chem 130:2182–2186. https://doi.org/10.1002/ange.201711357
138. Zhu M, Sun Z, Fujitsuka M, Majima T (2018) Z-scheme photocatalytic water splitting on a 2D heterostructure of black phosphorus/bismuth vanadate using visible light. Angew Chem Int Ed 57:2160–2164. https://doi.org/10.1002/anie.201711357
139. Li Z, Hou J, Zhang B et al (2019) Two-dimensional Janus heterostructures for superior Z-scheme photocatalytic water splitting. Nano Energy 59:537–544
140. Xu Q, Zhu B, Jiang C et al (2018) Constructing 2D/2D Fe_2O_3/g-C_3N_4 direct Z-scheme photocatalysts with enhanced H_2 generation performance. Sol Rrl 2:1800006
141. Liu D, Zhang S, Wang J et al (2019) Direct Z-scheme 2D/2D photocatalyst based on ultrathin g-C_3N_4 and WO_3 nanosheets for efficient visible-light-driven H_2 generation. ACS Appl Mater Interfaces 11:27913–27923
142. Xie H, Zhao Y, Li H et al (2019) 2D $BiVO_4$/g-C_3N_4 Z-scheme photocatalyst for enhanced overall water splitting. J Mater Sci 54:10836–10845
143. Shi J, Li S, Wang F et al (2019) In situ topotactic formation of 2D/2D direct Z-scheme Cu 2 S/Zn 0.67 Cd 0.33 S in-plane intergrowth nanosheet heterojunctions for enhanced photocatalytic hydrogen production. Dalt Trans 48:3327–3337
144. Shi J, Li S, Wang F et al (2018) In situ topotactic fabrication of direct Z-scheme 2D/2D ZnO/ZnxCd1−xS single crystal nanosheet heterojunction for efficient photocatalytic water splitting. Catal Sci Technol 8:6458–6467. https://doi.org/10.1039/C8CY01884G
145. Wang K, Jiang L, Wu X, Zhang G (2020) Vacancy mediated Z-scheme charge transfer in a 2D/2D $La_2Ti_2O_7$/gC_3N_4 nanojunction as a bifunctional photocatalyst for solar-to-energy conversion. J Mater Chem A 8:13241–13247

146. Zhu B, Cheng B, Fan J et al (2021) g-C_3N_4-based 2D/2D composite heterojunction photocatalyst. Small Struct 2:2100086. https://doi.org/10.1002/sstr.202100086
147. Qin M-Z, Fu W-X, Guo H et al (2021) 2D/2D heterojunction systems for the removal of organic pollutants: a review. Adv Colloid Interface Sci 297:102540. https://doi.org/10.1016/j.cis.2021.102540
148. Su Q, Li Y, Hu R et al (2020) Heterojunction photocatalysts based on 2D materials: the role of configuration. Adv Sustain Syst 4:2000130. https://doi.org/10.1002/adsu.202000130
149. Su J, Li G, Li X, Chen J (2019) 2D/2D heterojunctions for catalysis. Adv Sci 6:1801702. https://doi.org/10.1002/advs.201801702
150. Liu L, Hu P, Cui W et al (2017) Increased photocatalytic hydrogen evolution and stability over nanosheet g-C_3N_4 hybridized CdS core@shell structure. Int J Hydrog Energy 42:17435–17445. https://doi.org/10.1016/j.ijhydene.2017.02.171
151. Subudhi S, Paramanik L, Sultana S et al (2020) A type-II interband alignment heterojunction architecture of cobalt titanate integrated UiO-66-NH2: a visible light mediated photocatalytic approach directed towards Norfloxacin degradation and green energy (Hydrogen) evolution. J Colloid Interface Sci 568:89–105
152. Zou L, Wang H, Wang X (2017) High efficient photodegradation and photocatalytic hydrogen production of CdS/BiVO4 heterostructure through Z-scheme process. ACS Sustain Chem Eng 5:303–309. https://doi.org/10.1021/acssuschemeng.6b01628
153. Ma D, Shi J-W, Zou Y et al (2017) Rational design of CdS@ZnO core-shell structure via atomic layer deposition for drastically enhanced photocatalytic H2 evolution with excellent photostability. Nano Energy 39:183–191. https://doi.org/10.1016/j.nanoen.2017.06.047
154. Liu F, Shi R, Wang Z et al (2019) Direct Z-scheme hetero-phase junction of black/red phosphorus for photocatalytic water splitting. Angew Chem 131:11917–11921
155. Liu F, Shi R, Wang Z et al (2019) Direct Z-scheme hetero-phase junction of black/red phosphorus for photocatalytic water splitting. Angew Chem Int Ed 58:11791–11795. https://doi.org/10.1002/anie.201906416
156. Kramm UI, Marschall R, Rose M (2019) Pitfalls in heterogeneous thermal, electro- and photocatalysis. ChemCatChem 11:2563–2574. https://doi.org/10.1002/cctc.201900137
157. Wang Q, Hisatomi T, Jia Q et al (2016) Scalable water splitting on particulate photocatalyst sheets with a solar-to-hydrogen energy conversion efficiency exceeding 1%. Nat Mater 15:611–615. https://doi.org/10.1038/nmat4589
158. Kisch H (2015) Semiconductor photocatalysis. Wiley, New York
159. Abd-Rabboh HSM, Benaissa M, Hamdy MS et al (2021) Synthesis of an efficient, and recyclable mesoporous BiVO4/TiO2 direct Z-scheme heterojunction by sonochemical route for photocatalytic hydrogen production and photodegradation of rhodamine B dye in the visible region. Opt Mater (Amst) 114:110761. https://doi.org/10.1016/j.optmat.2020.110761
160. Guan R, Zhai H, Li J et al (2020) Reduced mesoporous TiO_2 with Cu_2S heterojunction and enhanced hydrogen production without noble metal cocatalyst. Appl Surf Sci 507:144772. https://doi.org/10.1016/j.apsusc.2019.144772
161. Maček Kržmanc M, Daneu N, Čontala A et al (2021) $SrTiO_3/Bi_4Ti_3O_{12}$ nanoheterostructural platelets synthesized by topotactic epitaxy as effective noble-metal-free photocatalysts for pH-neutral hydrogen evolution. ACS Appl Mater Interfaces 13:370–381. https://doi.org/10.1021/acsami.0c16253
162. Xing X, Zhu H, Zhang M et al (2018) Interfacial oxygen vacancy layer of a Z-scheme BCN–TiO 2 heterostructure accelerating charge carrier transfer for visible light photocatalytic H_2 evolution. Catal Sci Technol 8:3629–3637. https://doi.org/10.1039/C8CY01035H
163. Xie YP, Yang Y, Wang G, Liu G (2017) Oxygen vacancies promoted interfacial charge carrier transfer of CdS/ZnO heterostructure for photocatalytic hydrogen generation. J Colloid Interface Sci 503:198–204. https://doi.org/10.1016/j.jcis.2017.05.006
164. Liu J, Tao Z, Xie H et al (2019) Facial construction of defected NiO/TiO_2 with Z-scheme charge transfer for enhanced photocatalytic performance. Catal Today 335:269–277. https://doi.org/10.1016/j.cattod.2018.11.055
165. Tian B, Tian B, Smith B et al (2018) Supported black phosphorus nanosheets as hydrogen-evolving photocatalyst achieving 5.4% energy conversion efficiency at 353 K. Nat Commun 9:1397. https://doi.org/10.1038/s41467-018-03737-4
166. Meng A, Zhu B, Zhong B et al (2017) Direct Z-scheme TiO2/CdS hierarchical photocatalyst for enhanced photocatalytic H_2-production activity. Appl Surf Sci 422:518–527. https://doi.org/10.1016/j.apsusc.2017.06.028

167. Qiu B, Zhu Q, Du M et al (2017) Efficient solar light harvesting CdS/Co9S8 hollow cubes for Z-scheme photocatalytic water splitting. Angew Chem 129:2728–2732. https://doi.org/10.1002/ange.201612551
168. Qiu B, Zhu Q, Du M et al (2017) Efficient solar light harvesting CdS/Co9S8 hollow cubes for Z-scheme photocatalytic water splitting. Angew Chem Int Ed 56:2684–2688. https://doi.org/10.1002/anie.201612551
169. Li X, Xie K, Song L et al (2017) Enhanced photocarrier separation in hierarchical graphitic-C_3N_4-supported CuInS2 for noble-metal-free Z-scheme photocatalytic water splitting. ACS Appl Mater Interfaces 9:24577–24583. https://doi.org/10.1021/acsami.7b06030
170. Rauf A, Ma M, Kim S et al (2018) Mediator-and co-catalyst-free direct Z-scheme composites of Bi 2 WO 6–Cu 3 P for solar-water splitting. Nanoscale 10:3026–3036
171. Yuan Q, Liu D, Zhang N et al (2017) Noble-metal-free janus-like structures by cation exchange for Z-scheme photocatalytic water splitting under broadband light irradiation. Angew Chem 129:4270–4274. https://doi.org/10.1002/ange.201700150
172. Yuan Q, Liu D, Zhang N et al (2017) Noble-metal-free janus-like structures by cation exchange for Z-scheme photocatalytic water splitting under broadband light irradiation. Angew Chem Int Ed 56:4206–4210. https://doi.org/10.1002/anie.201700150
173. Zou Y, Shi JW, Ma D et al (2017) Fabrication of g-C3N4/Au/C-TiO2 hollow structures as visible-light-driven Z-scheme photocatalysts with enhanced photocatalytic H2 evolution. ChemCatChem 9:3752–3761
174. Wang J, Wang G, Wang X et al (2019) 3D/2D direct Z-scheme heterojunctions of hierarchical TiO2 microflowers/g-C_3N_4 nanosheets with enhanced charge carrier separation for photocatalytic H2 evolution. Carbon N Y 149:618–626. https://doi.org/10.1016/j.carbon.2019.04.088
175. Cai H, Wang B, Xiong L et al (2019) Orienting the charge transfer path of type-II heterojunction for photocatalytic hydrogen evolution. Appl Catal B Environ 256:117853
176. Zhou BX, Ding SS, Wang Y et al (2020) Type-II/type-II band alignment to boost spatial charge separation: A case study of g-C3N4 quantum dots/a-TiO2/r-TiO2 for highly efficient photocatalytic hydrogen and oxygen evolution. Nanoscale 12:6037–6046. https://doi.org/10.1039/d0nr00176g
177. Pan J, Dong Z, Wang B et al (2019) The enhancement of photocatalytic hydrogen production via Ti_{3+} self-doping black TiO2/g-C_3N_4 hollow core-shell nano-heterojunction. Appl Catal B Environ 242:92–99
178. Jiang E, Song N, Che G et al (2020) Construction of a Z-scheme MoS_2/$CaTiO_3$ heterostructure by the morphology-controlled strategy towards enhancing photocatalytic activity. Chem Eng J 399:125721. https://doi.org/10.1016/j.cej.2020.125721
179. Liu Y, Zhang H, Ke J et al (2018) 0D (MoS2)/2D (g-C_3N_4) heterojunctions in Z-scheme for enhanced photocatalytic and electrochemical hydrogen evolution. Appl Catal B Environ 228:64–74. https://doi.org/10.1016/j.apcatb.2018.01.067
180. Xu F, Zhang L, Cheng B, Yu J (2018) Direct Z-scheme TiO2/NiS core–shell hybrid nanofibers with enhanced photocatalytic H2-production activity. ACS Sustain Chem Eng 6:12291–12298
181. Liang Y-H, Liao M-W, Mishra M, Perng T-P (2019) Fabrication of Ta_3N_5ZnO direct Z-scheme photocatalyst for hydrogen generation. Int J Hydrogen Energy 44:19162–19167. https://doi.org/10.1016/j.ijhydene.2018.07.117
182. Guo H-L, Du H, Jiang Y-F et al (2017) Artificial photosynthetic Z-scheme photocatalyst for hydrogen evolution with high quantum efficiency. J Phys Chem C 121:107–114. https://doi.org/10.1021/acs.jpcc.6b10013
183. Zhang W, Hu Y, Yan C et al (2019) Surface plasmon resonance enhanced direct Z-scheme TiO 2/ZnTe/Au nanocorncob heterojunctions for efficient photocatalytic overall water splitting. Nanoscale 11:9053–9060